Impact of permeability evolution in igneous sills on hydrothermal flow and hydrocarbon transport in volcanic sedimentary basins

Ole Rabbel[1,*], Jörg Hasenclever[2], Christophe Y. Galerne[3], Olivier Galland[1], Karen Mair[1], Octavio Palma[4]

[1] NJORD, Department of Geosciences, University of Oslo, Norway

[2] Institute of Geophysics, Center for Earth System Research and Sustainability, University of Hamburg University, Germany

[3] Faculty of Geosciences, University of Bremen, Germany

[4] Facultad de Ciencias Naturales y Museo, Universidad de La Plata, Argentina

correspondence to: ole.rabbel@gmail.com

Abstract:

Sills emplaced in organic-rich sedimentary rocks trigger the generation and migration of hydrocarbons in volcanic sedimentary basins. Based on seismic and geological observations, numerical modeling studies of hydrothermal flow around sills show that thermogenic methane is channeled below the intrusion towards its tip, where hydrothermal vents nucleate and transport methane to the surface. However, these models typically assume impermeable sills and ignore potential effects of permeability evolution in cooling sills, e.g., due to fracturing. Here, we combine a geological field study of a volcanic basin (Neuquén Basin, Argentina) with hybrid FEM/FVM numerical modeling of hydrothermal flow around a sill, including hydrocarbon generation and transport. Our field observations show widespread veins within sills composed of graphitized bitumen and cooling joints filled with solid bitumen or fluidized shale. Raman spectroscopy indicates graphitization at temperatures between 350-500°C, suggesting fluid flow within the intrusions during cooling. This finding motivates our modeling setup, which investigates flow patterns around and through intrusions that become porous and permeable upon solidification. The results show three flow phases affecting the transport of hydrocarbons generated in the contact aureole: (1) Contact-parallel flow toward the sill tip prior to solidification, (2) upon complete solidification, sudden vertical "flushing" of overpressured hydrocarbon-rich fluids from the lower contact aureole towards and into the hot sill along its entire length, and (3) stabilization of hydrocarbon distribution and fading hydrothermal flow. In low-permeability host rocks, hydraulic fracturing facilitates flow and hydrocarbon migration toward the sill by temporarily elevating porosity and permeability. Up to 7.5% of the generated methane is exposed to temperatures >400°C in the simulations and may thus be permanently stored as graphite in or near the sill. Porosity and permeability creation within cooling sills may impact hydrothermal flow, hydrocarbon transport and venting in volcanic basins, as it considerably alters the fluid pressure configuration, provides vertical flow paths, and helps to dissipate overpressure below the sills.

1 Introduction

Sill intrusions emplaced in sedimentary rocks strongly influence generation and migration of hydrocarbons and greenhouse gases in volcanic sedimentary basins. If sill intrusions are emplaced in organic-rich strata, they trigger contact-metamorphic reactions (e.g., organic matter transformation), overpressure generation and hydrothermal fluid flow in the surrounding strata (Einsele et al., 1980; Aarnes et al., 2012). Many recent studies of volcanic sedimentary basins investigate how such processes may cause the formation of hydrothermal vent complexes, which facilitate greenhouse gas release to the atmosphere and can thus drive global climate change (Svensen et al., 2004; Aarnes et al., 2010; Aarnes et al., 2012; Iyer et al., 2013; Iyer et al., 2017; Galerne and Hasenclever, 2019). Additionally, the same processes can be critical factors for hydrocarbon generation and migration in igneous petroleum systems containing sills emplaced within shale formations (Senger et al., 2017; Spacapan et al., 2020).

Hydrothermal flow in response to intrusion of magma into sedimentary host rocks has been investigated for decades. The magmatic heat input leads to several temperature-dependent processes that promote strong fluid pressure increase, which drive fluid flow (Einsele et al., 1980; Delaney, 1982). These processes include for instance thermal fluid expansion, mineral dehydration, organic matter transformation into hydrocarbon generation, and pore space reduction due to mineral precipitation (Einsele et al., 1980; Delaney, 1982; Aarnes et al., 2010; Townsend, 2018). When the rate of overpressure generation is larger than flow-driven pressure dissipation, e.g., in low-permeable rocks like shale, hydraulic fractures form and locally enhance fluid flow and pressure release (Jamtveit et al., 2004; Aarnes et al., 2012; Kobchenko et al., 2014; Panahi et al., 2018; Rabbel et al., 2020). This process may lead to explosive hydrothermal vents, which are present in several volcanic basins (Nermoen et al., 2010; Aarnes et al., 2012; Iyer et al., 2017). In general, Ingebritsen et al. (2010) highlighted the deciding role of permeability structure for magmatic hydrothermal systems, where permeability of 10^{-16} m^2 represents the approximate boundary between convection and conduction dominated systems.

Numerical models simulate these coupled processes to understand hydrothermal flow dynamics and the associated hydrocarbon migration (usually represented as methane carried in the hydrothermal fluids). Typically, these models investigate potential vent formation around sills emplaced in organic-rich sediments. Such simulations usually assume that sills are impermeable and show that vents seem to preferentially form at the inclined tips of large "saucer-shaped" sills, because fluids get trapped under the sill and migrate towards their tips. This situation favours both fast fluid pressure build-up below the sills and focussed fluid migration towards the tips (Iyer et al., 2013, Iyer et al., 2017; Galerne and Hasenclever, 2019).

However, observations from several volcanic sedimentary basins indicate that the assumption of impermeable sills is not generally valid. Sills often host fracture networks including different fracture types. These form shortly after solidification of the magma and may include columnar cooling joints or fractures related to thermal contraction or hydraulic fracturing during hydrothermal activity (Senger et al. 2015, Witte et al. 2012, Rabbel et al., 2021). Multiple studies have provided evidence that such fracture networks may be open and can contain water (Chevallier et al., 2004) or hydrocarbons and act as fluid pathways or even fractured reservoirs (Mark et al., 2018; Schofield et al., 2020; Spacapan et al., 2020).

Mainly based on evidence from field and subsurface data, several studies hypothesized that cooling-related fracturing in sills creates an early migration pulse of fluids into the sill, although the thermal regime of such a pulse is under debate (Witte et al., 2012, Spacapan et al. 2020, Rabbel et al. 2021). In addition, Spacapan et al. (2019) noted the absence of hydrothermal vents around the sills in the Neuquén Basin and suggested that pore pressures were not high enough to create such features. A recent study on the Karoo Basin in South Africa estimates that half of the thermogenic gas mobilized in the contact aureole of flat sills may enter the sill through cooling joints (Lenhard et al., 2023). Although based on field evidence, these geological models remain qualitative in terms of the physical process dynamics, and a dedicated study to investigate quantitative hydrothermal flow and hydrocarbon migration around and in fractured, permeable sills is currently missing.

In this study, we combine a field study from the Neuquén Basin, Argentina, with numerical modelling to: (1) investigate if and in which thermal conditions opening of cooling joints may trigger an early hydrocarbon migration pulse into the sill, and (2) assess the impact of porosity and permeability generation in sills on the hydrothermal flow and hydrocarbon migration and storage in comparison to systems with impermeable sills. The northern Neuquén Basin provides well documented examples of sills with extensive cooling joint networks emplaced in organic-rich shale, many of which are commercial oil reservoirs (Rodriguez Monreal et al., 2009; Witte et al., 2012; Spacapan et al., 2020). Additionally, the strong thermal impact of intrusions on host rock maturation in these systems is well documented (Rodriguez Monreal et al., 2009; Spacapan et al., 2018). We first present geological evidence for hydrocarbon transport through fractured sills in a hydrothermal environment. Our field observations motivate a numerical modelling study to investigate the influence of cooling joint formation, i.e., permeable sills, on the hydrothermal flow patterns and hydrocarbon migration. We perform simulations for sills emplaced in host rocks of different permeability to be able to discuss the effect for different geological settings. By integrating the simulations results with geological evidence, we show how permeable sills affect hydrothermal flow in volcanic sedimentary basins as well as the fate of hydrocarbons generated by contact-metamorphism.

2 Geological observations

2.1 Geological setting

The study area is located around the Río Grande Valley (RGV) in the northern Neuquén Basin, Argentina, about 100 km south of the town of Malargüe (Figure 1). The Neuquén Basin initially formed as a series of isolated half-grabens during the late Triassic to early Jurassic (Howell et al., 2005). During the middle Jurassic to early Cretaceous, these depocenters coalesced during thermal subsidence, forming a large shallow-marine basin. This phase included the deposition of the Vaca Muerta and Agrío formations, which comprise several hundreds of meters of calcareous, organic-rich shale and form two important source rock formations for presently exploited petroleum systems (Kietzmann et al., 2014). From the early Cretaceous, the basin developed into a foreland basin in response to the compressive tectonic regime of the Andean orogeny. This led to inversion of the Triassic normal faults and generation of a series of fold-thrust belts along the western basin boundary (Manceda and Figueroa, 1995; Yagupsky et al., 2008).

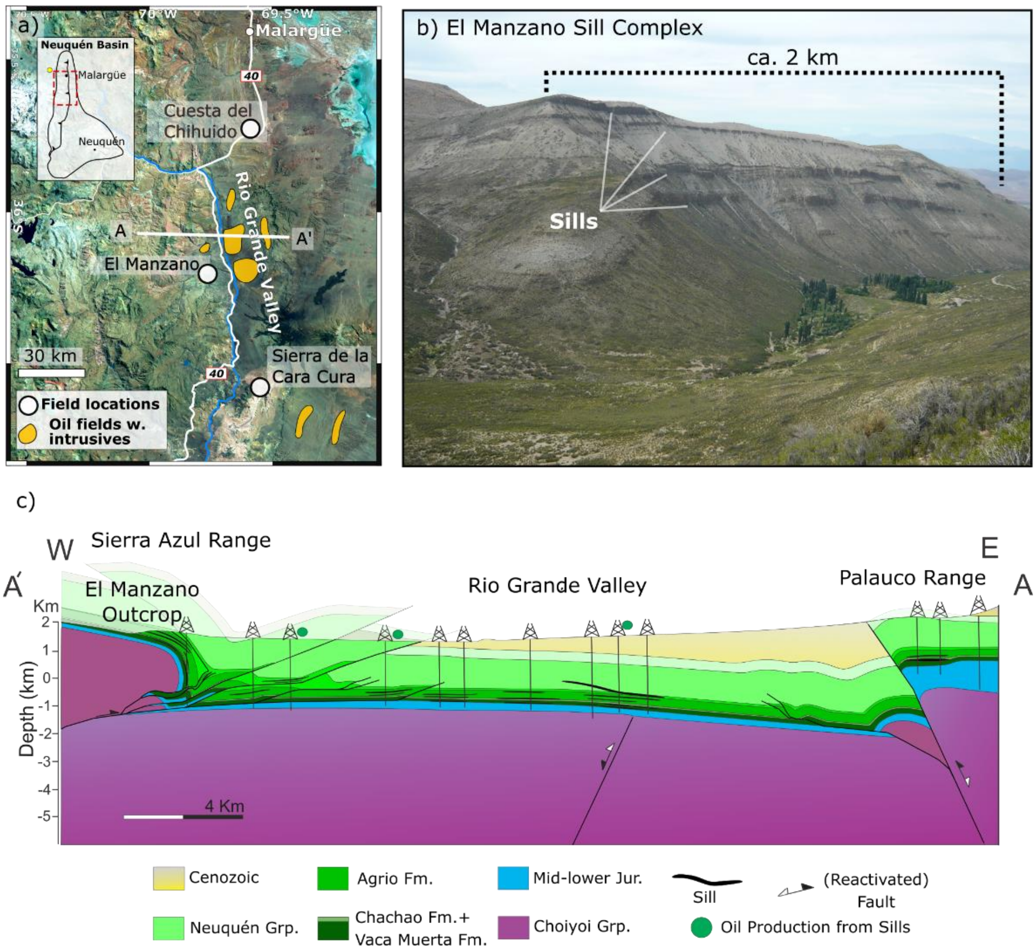

Figure 1. (a) Satellite image (Landsat, courtesy USGS) of the study area in the northern Neuquén Basin including field localities (white dots) and producing igneous petroleum systems (green areas). (b) View of the El Manzano sill complex outcrop in the Sierra Azul range (Photo: F. Soto). (c) E-W structural geological section illustrating the relation between subsurface and outcropping sill complexes (courtesy. J. B. Spacapan)

In addition to tectonic deformation, the northern Neuquén Basin experienced intense magmatic activity that formed a series of volcanic plateaus and widespread magmatic intrusions within the sedimentary succession (Kay et al., 2006). In the study area, two main eruptive cycles, termed Molle and Huincán eruptive cycles, occurred in the late Oligocene-mid Miocene and the late Miocene-Pleistocene, respectively (Combina and Nullo, 2005). These events led to the emplacement of extensive andesitic and basaltic sill complexes predominantly in the Vaca Muerta and Agrío Formations, but also in overlying gypsum and sandstone units (Spacapan et al., 2020).

In the RGV, heavily fractured sills emplaced in the Vaca Muerta and Agrío formations constitute the reservoirs in an actively producing igneous petroleum system (Schiuma, 1994; Witte et al., 2012). Spacapan et al. (2020) reported 2 to 27 m thick sills in these shale formations, but up to 54 m within shallower clastic sediments of RGV. Other studies from the northern Neuquén Basin report thick laccolith intrusions (>100 m) acting as reservoirs (Rodriguez Monreal et al., 2009). Spacapan et al. (2018) showed that the heat input provided by the sills matured the Vaca Muerta and Agrío shale formations, which otherwise show very low thermal maturity at burial depths of ca. 2-2.5 km. The established model for the formation of these igneous reservoirs includes that the intrusions developed interconnected cooling joint networks, which subsequently stored the generated hydrocarbons (Witte et al., 2012; Spacapan et al., 2020).

In addition to the subsurface sill complexes, thrust tectonics brought to surface exceptional analogue outcrops in the surrounding mountain ranges including the Sierra Azul, Sierra Cara Cura and Cuesta del Chihuido (Figure 1). Several studies describe these localities, which offer easy access to sills emplaced in the Vaca Muerta and Agrio formations (Spacapan et al., 2017; Rabbel et al., 2018; Rabbel et al., 2021). Especially the km-scale outcrops at El Manzano (Figure 1b) and Sierra Cara Cura constitute direct analogues to the subsurface sill complexes of RGV igneous petroleum system (Palma et al., 2019; Rabbel et al., 2021). These three field localities are ideal case studies to reveal the interactions between igneous intrusions and the petroleum system.

2.2 Geological field observations

During three field campaigns, we collected an extensive dataset at outcrops in El Manzano, Sierra de la Cara Cura and Cuesta del Chihuido (Figure 1). We gathered ground-based and drone digital photographs to document outcrop observations. Additionally, we collected over 100 rock samples from the intrusions, surrounding shale as well as various types of veins for geochemical analyses. Note that a more comprehensive description of the field study is presented by Rabbel et al. (2021).

2.3 Observations of hydrocarbons inside and around sills

Outcropping sills in all three localities feature solid bitumen and black shale inside the fracture network of the sills. At Cuesta del Chihuido, both the side and roof of thin sills are exposed, and the side view reveals upwelling dykelets of black shale (Vaca Muerta Formation) entering the sill from the bottom contact (Figure 2a). The top view of the same sill shows the entire polygonal cooling joint network with a black fill of the same material (Figure 2a, b). Brecciated igneous material often surrounds the dykelets where they enter the intrusion.

The larger sills at El Manzano (Sierra Azul) and Sierra Cara Cura also show widespread bitumen in the fracture network of the sills, but at a much larger scale (Figure 3). We observe arrays of 1-up to 50 cm thick and >10 m high bitumen dykes or veins (Figure 3a). Here, the bitumen dyke cuts across the contact aureole and enters the sill intrusion. We find exposures of similar structures where the sill interior is accessible (Figure 3b). The sill appears heavily fractured in addition to preexisting cooling joints, and solid bitumen or calcite fill nearly all fractures. On closer inspection, the bituminous material in these veins has a shiny and fibrous texture.

At an exposed sill tip at El Manzano, we also observe that several cm thick bitumen veins appear to be concentrated along the tip contact, where they mutually cross-cut with calcite veins of at least similar thicknesses (Figure 3c, d). These calcite veins have cm-scale pores, which occasionally contain solid bitumen themselves and release strong hydrocarbon smell when the vein is broken up.

2.4 Bitumen characterization

The fibrous texture of the observed bitumen within the sills is intriguing and we hypothesized that it may be much higher-grade bituminous material than that described in the Neuquén basin and commonly attributed to regional burial (Parnell et al., 1995; Cobbold et al., 1999; Zanella et al., 2015).

In the field, we tested this hypothesis by measuring the resistivity of the fibrous bitumen with a hand-held multimeter. Graphitization of bitumen significantly changes the electric resistivity of the material: amorphous solid bitumen is very resistive and used as an electric insulator in industry applications (Hays et al., 1967), while graphite is an excellent conductor. Qualitative on-site resistivity measurements showed that the fibrous bitumen conducts electric currents well, i.e., within the detection limit of a standard multimeter, suggesting significant graphitization.

In addition, we applied Raman spectroscopy to better constrain the nature of the solid bitumen and its thermal history. Raman spectroscopy provides positions and relative intensities of spectral peaks characterizing carbonaceous materials like bitumen, including D ("disorder") and G ("graphite") peaks at 1345 cm^{-1} and 1585 cm^{-1}, respectively (Potgieter-

Vermaak et al., 2011; Rantitsch et al., 2016). The shape of the spectra and the D/G peak and area ratios allow a classification of high-grade alteration of the bitumen to anthracite or (semi-)graphite and may serve as a geothermometer for high-temperature regimes (Beyssac et al., 2002; Rantitsch et al., 2016). Due to the high temperatures within and around igneous intrusions, we expect this method to give an indication on the degree of thermal alteration and thus temperatures that the hydrocarbons experienced. Since Raman spectra can show varying absolute intensities, we normalized each spectrum to the intensity of the respective G peak (I_G) for visualization purposes.

Raman spectrograms of the sampled bitumen veins show very clearly developed G and D1 peaks and I_{D1}/I_G ratios of ca. 1 and 0.9, respectively (Figure 4). The D3 band between the peaks is nearly absent in the sample from Sierra de la Cara Cura (from vein in Figure 3b), while it is visible at low intensity in the presented sample from El Manzano (from vein in Figure 3a). Note that both vein samples stem from the intrusion-host contact, and each veins penetrate about 10 m into around 20 m thick sills.

Figure 2. Field observations of upwelling dykelets of liquefied shale and bitumen entering the cooling joint network of a thin sill at Cuesta del Chihuido (ca. 30 cm thick). (a) Side view showing the sediment-intrusion contact and dyke (Photo: D. Michelon), (b) top view demonstrating black bituminous fill in the polygonal cooling joints.

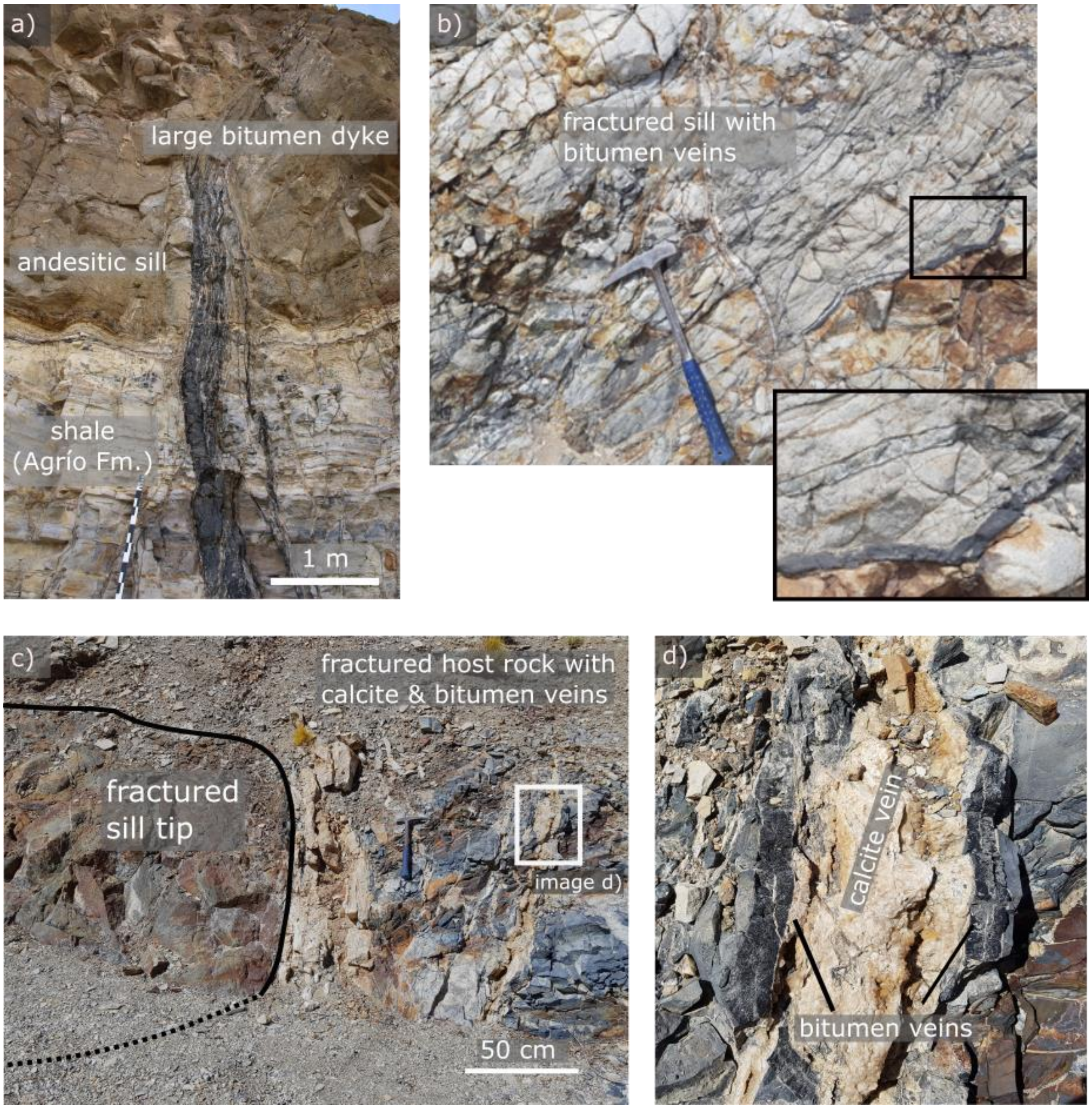

Figure 3. Examples of dykes or veins of solid bitumen associated the sill intrusions. (a) Bitumen dyke at El Manzano of >10 m height and up to 0.5 m thickness originating in the aureole of Agrío Fm. and entering the sill through the bottom contact. (b) Fractured zone inside a sill at Sierra de la Cara Cura exhibiting many cm-scale veins of solid bitumen. (c, d) Exposed sill tip at El Manzano showing high concentration of fibrous bitumen and calcite veins in the contact in front of the tip.

2.5 Composition and thermal implications of bitumen samples

We compare our Raman results with those measured in carbonaceous material from several studies, where increased graphitization and metamorphism lead to well-developed, narrow graphite (G) and disordered carbon (D1) peaks, weak or absent D3 bands, and I_G/I_D peak ratios of <1 (Beyssac et al., 2002; Kwiecinska et al., 2010; Rantitsch et al., 2016). Although we did not perform quantification via peak-fitting, a qualitative comparison of our results with highly metamorphosed sediments presented by Beyssac et al. (2002, Fig. 6 and 11) leads to estimated temperatures of 350-500°C for our samples (Figure). Hydrothermal graphitization can occur along intrusion-sediment contacts at relatively shallow crustal levels and requires temperatures of >= 400°C (Buseck and Beyssac, 2014). Hydraulic fracturing focuses the flow of hydrothermal fluids oversaturated with CH_4 and/or CO_2 from which crystalline graphite may precipitate (Rumble, 2014). This fits well with the observations that the bitumen dykes in our study area consist of pure, often crystalline graphitic material and occupy fractured zones in the aureole, around the intrusion tip, or within the sills themselves (Figure 3). In a previous summary of fracture types present in the sills of the study area, Rabbel et al. (2021) interpreted these features as hydraulic fractures. Thus, evidence from graphitized bitumen in the fractures in the aureole and in the sills, themselves points to hydrocarbon transport in a high-pressure, high-temperature environment in which at least part of the mobilized carbon transforms to graphitic carbonaceous material.

Our field and sample results strongly suggest that significant volumes of hydrocarbons circulated through the sills when the temperature at their margins were 350-500°C. The temperature was thus likely much higher in the interior of the sills. We infer that hydrothermal flow also occurred along cooling fractures within the sill, i.e., the sill developed some permeability while still hot (cf. Figure 2). This interpretation challenges the common assumption of previous models of hydrothermal circulation around cooling sills that intrusions remain impermeable during cooling (Aarnes et al., 2012; Iyer et al., 2017, Galerne & Hasenclever, 2019). An exception is the study of Iyer et al. (2013), who tested a model that included a linear permeability increase inside a cooling sill. While the author highlighted the importance of this mechanism in potentially facilitating the upward migration of thermogenic gas generated beneath sills, this test remained exploratory. Hence, no great detail analyses on the effect on the hydrothermal flow is provided nor supported by field evidence. Thus, a dedicated modeling study on the effect of permeability creation in cooling sills on hydrothermal flow and hydrocarbon transport is still missing. In the following section, we therefore present numerical simulations to test the effects of permeability increase associated with fracturing within the sills on hydrothermal circulations, and how this affects hydrothermal transport of hydrocarbons around sills.

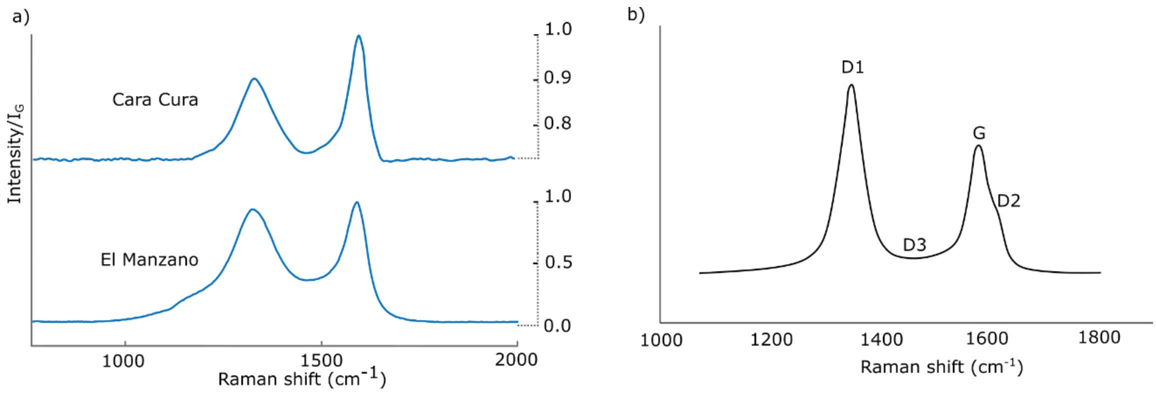

Figure 4. (a) Raman spectra from two bitumen vein samples at Sierra de la Cara Cura and El Manzano, respectively. Both samples include well-developed and narrow graphite and disordered carbon (G, D1) peaks as well as weak or absent D3 band. (b) Reference Raman spectrum to illustrate spectra decomposition of carbonaceous material after Beyssac et al. (2002).

3 Numerical Simulations

3.1 Model description

We employ the two-dimensional (2D) finite element model of Galerne and Hasenclever (2019), who applied it to quantify degassing through sill-related hydrothermal vents. The model is presented in detail in Galerne and Hasenclever (2019). Here we will limit our discussion to the main features and point out the key adjustments made for this study. In short, the model simulates hydrothermal flow around a cooling sill, but is also coupled to a model for the heat-driven chemical transformation of organic matter into hydrocarbons (represented by methane). This allows us to investigate not only hydrothermal circulation around sills as such, but also how this affects transport of the hydrocarbons generated in the contact aureole.

The model considers single-phase hydrothermal flow of a compressible fluid in a porous medium following Darcy's law. Temperature calculations comprise heat diffusion, heat advection and heat sources/sinks related to latent heat of magma crystallization, mineral dehydration, thermal cracking of organic matter as well as internal fluid friction and pressure-volume work. Fluid density varies with temperature and pressure according to the equation of state of pure water. The pore pressure equation also contains source terms representing fluid release due to temperature-dependent, irreversible contact metamorphic reactions, including (i) organic matter transformation into methane and (ii) clay mineral dehydration.

To calculate organic matter transformation to light hydrocarbon, the model uses the EASY%Ro method (Sweeney and Burnham, 1990), which quantifies the converted fraction of organic matter and thermal maturity through vitrinite reflectance *Ro*. Here we assume that all organic matter transformation is converted to methane. We monitor transport and accumulation of the released methane due to hydrothermal flow using a finite volume advection scheme, but do not consider buoyancy effects resulting from the addition of methane to the pore fluid. Clay mineral dehydration follows the maximum storable weight fraction of water in the stable mineral assemblage at a given temperature, which is predicted by phase equilibria (Connolly, 2009). This process not only produces additional pore fluid, but also causes a permanent porosity increase in the affected host rock to ensure mass conservation of rock and fluid. The brittle-ductile transition for the host rock is assumed to happen at 500-750°C and linearly decreases permeability (Galerne and Hasenclever, 2019). Note here that while the model calculations are conducted with methane properties, the results can be used to understand transport of (light) hydrocarbons around sills in general. We thus use "methane" and "hydrocarbons" interchangeably in the context of this study.

The model provides time series of the 2D fields of all relevant rock properties in the model domain and physical quantities related to metamorphism and hydrothermal flow. Since we investigate the impact of permeable sills on the fluid and hydrocarbon circulation, our analysis focuses on visualization of the temperature, permeability, fluid flow and methane accumulation during cooling of the sill.

3.2 Adjustments for this study

We adjusted three aspects of the original model to honor geological observations in the study area. First, we limit rock failure to tensile hydraulic fracturing and do not consider shear failure. We assume that hydrofracturing occurs at sufficiently high pore fluid overpressure, i.e., if pore pressure exceeds the sum of lithostatic stress and tensile strength. Here, we consider hydrofracturing of the host rock and not within the sill.

Second, we assume that hydrofracturing increases not only permeability but also porosity, which is often neglected in numerical models for simplicity. However, the additional space provided by the opening of hydraulic fractures, which we approximate by the porosity increase, is an important storage buffer during thermal expansion of fluids and hydrocarbon generation. While a transient permeability increase during hydrofracturing can easily be defined without affecting the numerical stability and physical plausibility of the model, prescribing a porosity increase associated with hydrofracturing is not straightforward. A prescribed too large porosity increase, for instance, would create a strong suction effect leading to unrealistically low pressures or even underpressure. We solve this problem by iteratively increasing porosity in regions where overpressure exceeds the failure criterion and solving again for the pore pressure field until a consistent solution establishes, which on average requires 10 – 15 iterations. Hydrofracturing is treated reversible and its effects on porosity and permeability vanish once pore pressure drops below the failure criterion. In this study, we limit the hydrofracturing-related maximum porosity and permeability increase to 1% and a factor 100, respectively.

Third, we approximate the process of cooling joint formation within the sill through a linear temperature-dependent permanent increase of permeability, similar to Iyer et al. (2013), but additionally consider the corresponding permanent porosity increase. Note that this is likely a strong simplification of fracture flow through cooling joints networks, which is still poorly constrained. Bulk volume reduction of the cooling and crystallizing magma induces thermal stresses that lead to the formation of a cooling joint network, creating primary porosity and permeability inside the intrusion (e.g., Petford, 2003; Hetényi et al., 2012). The overall pore-space gained in our model is set to equate 8% volume loss, occurring during the transition from a melted to crystallized magma (between the liquidus and solidus temperature), based on reported fracture porosities from fractured sill reservoirs in the study area (Witte et al., 2012; Spacapan et al., 2020). To be consistent with the crystal-mush model described by Marsh (2002), the onset of the pore opening should be when 50-55% of the magma has crystallized. Here we take a value of 1000°C as the onset of the brittle-ductile-transition (BDT) temperature. Using a linearized, temperature-dependent definition of the melt fraction, $(T-T_S)/(T_L-T_S)$, with $T_L = 1100°C$ and $T_S = 900°C$ being liquidus and solidus temperatures, respectively, the set value for the BDT in our simulations implies that cooling joint creation starts at 1000°C when, at any distance from the sill margins, 50% of the sill has crystallized (Figure 5c).

Note that we limit the model's representation of fracturing in the sill to cooling joints and thus perform a strong simplification compared to the complex interplay of thermal and hydraulic fracturing mechanisms observed in the field (cf. section 3 and Rabbel et al, 2021). However, the goal is to study the general impact of porous and permeable sills on hydrothermal flow and the associated hydrocarbon transport and storage, which is possible even with this limitation.

3.3 Modeling setup

Our modeling setup consists of a single flat sill of 50 m thickness and 1 km length emplaced at 3 km depth in a homogenous host rock (Figure 5a). We performed a parameter sensitivity study to investigate the impact of porosity and permeability development in sills emplaced in either low-permeability (e.g., shale) and high-to-medium permeability (e.g., silt-/sandstone) host rocks. This allows us to investigate the sills of our study area (sills in Agrío and Vaca Muerta shales), but also compare to sills in the overlying Neuquén Group (silt-/ sandstones) or other relevant geological settings. Figure 5 and Table 1 show the model setup and the list of important model parameters, respectively. Note that we also carried out simulations with thinner sills and provide those as supplementary data for completeness, but do not address their results in detail. We first conducted a series of reference setups including permanently impermeable sills emplaced in either high- or low-permeable host rock. Subsequently, we use the same setups but activate temperature-dependent porosity and permeability generation for the sills. Hydraulic fracturing of the host rock is activated in all simulations.

The model domain (Figure 5a) is 4000 m wide, extends from the surface to 1000 m below the emplacement depth of the sill and is discretized with a triangular mesh with variable element sizes between 0.5 - 50 m (smallest around and within the sill, see Figure 5c). We assume instantaneous sill emplacement at 1100°C, corresponding to the inferred liquidus temperatures of andesitic magma in the study area (Spacapan et al., 2018). The left and right boundaries are insulating and impermeable, and we calibrated the fixed temperature at the impermeable bottom boundary to create a geothermal gradient of around 25 °C/km. The top boundary mimics the behaviour of a shallow seafloor with temperature set to 10 °C, pressure set to 0.1 MPa and free in- and outflow. Otherwise, initial conditions consider no basin history such as uplift and erosion, and no pre-existing thermal maturation prior to sill emplacement. We justify this by low background maturity values reported in the study area (Spacapan et al., 2018; Palma et al., 2019; Rabbel et al., 2021).

For the sediments, we chose a homogenous material with 5% TOC and ca. 5 weight percent bound water, as well as exponential decay of porosity with depth (Figure 5b). Permeability is porosity-dependent and follows a Kozeny-Carman relationship. This relationship is calibrated to values of low-permeability Agrio and Vaca Muerta shale formations at 2-3 km depth in the northern Neuquén Basin, yielding 10^{-18} m^2 at 3 km. This corresponds to emplacement depths for the igneous petroleum systems present in both subsurface and outcrop (Figure 5b). To compare with settings with more permeable lithologies (silt-/sandstone), we increased the host rock permeability by two orders of magnitude for another set of simulation (Figure 5b). Yet, each host rock setup remains a simplification, as we do not include lithological variations. Sill permeability starts at 10^{-20} m^2 (impermeable) and increases to 10^{-15} m^2 at 900°C. In lack of macroscopic permeability measurements, we chose the maximum permeability value to approximate the upper range for Neuquén sill reservoirs as reported by Spacapan et al. (2020). These values were obtained from (micro-)fractured sill matrix samples and therefore likely underestimate bulk permeability, as they do not include macroscopic cooling joints.

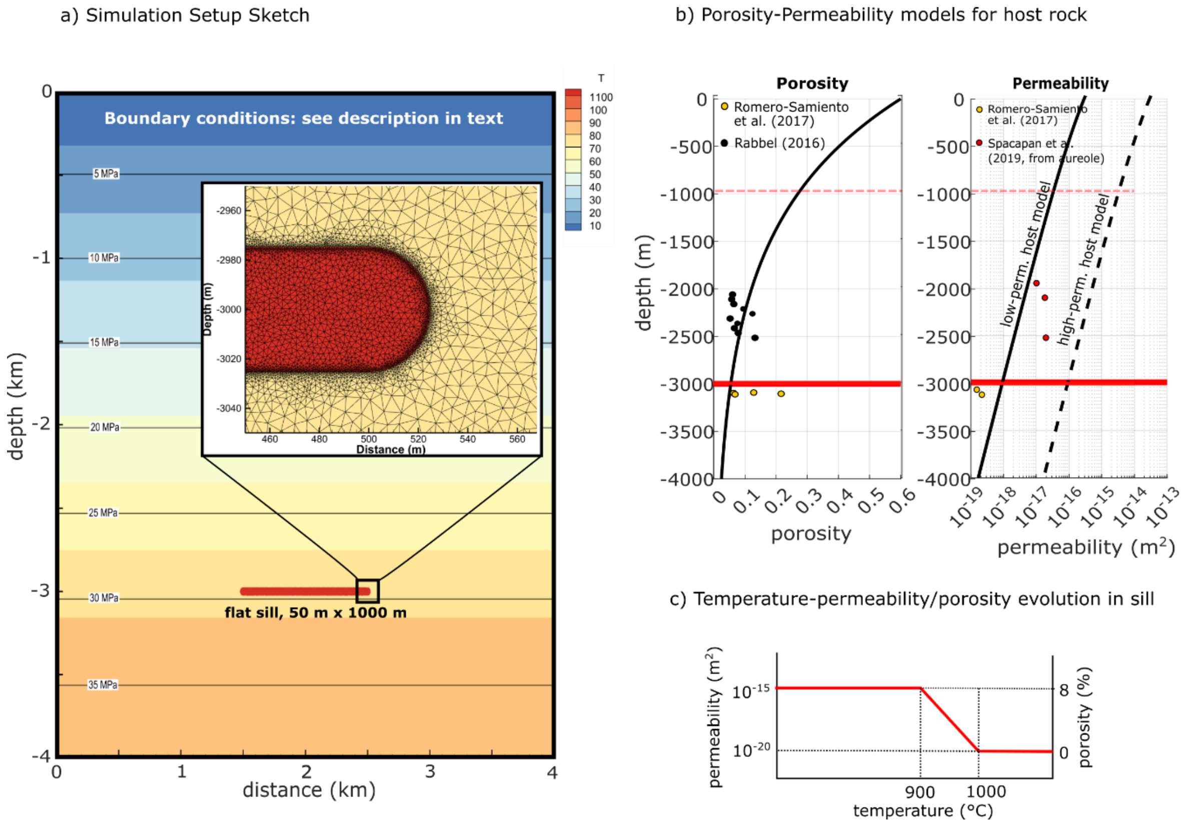

Figure 5. Illustration of the numerical modelling setup. (a) Model domain, with initial temperature and pore pressure field and close-up for mesh illustration. (b) Porosity-permeability-depth relationships in the models alongside reported data from the Vaca Muerta formation from various depths (Rabbel 2017, Romero-Samiento et al. 2017, Spacapan et al. 2019). Note that permeabilities from Spacapan et al. (2019) are the smallest values reported from the fractured and altered aureole of sills and thus likely overestimating background values. (c) Illustration of porosity-permeability-temperature function for sill with assumed cooling joint formation.

Table 1. Material properties used for hydrothermal simulations

Fixed rock parameters	Value	Unit
Fluid Properties	Equation of state for pure water (IAPS-84)	
Magma / Sill Properties (representing andesite)		
Specific heat capacity[1,2]	900	$J\ kg^{-1}\ K^{-1}$
Latent heat of crystallization[1,2]	320	$kJ\ kg^{-1}$
Initial sill temperature[3,4]	1100	°C
Liquidus temperature[3]	1100	°C
Solidus temperature[4]	900	°C
Brittle-Ductile-Transition (permeability creation)	1000-900	°C
Sill thickness[4]	50 (+ 10 in supplement)	m
Density[2,6]	2830	$kg\ m^{-3}$
Thermal conductivity[5]	2.51	$W\ m^{-1}\ K^{-1}$
Permeability range in sill[7]	$10^{-20} – 10^{-15}$	m^2
Porosity range in sill[7]	0 – 0.08	1
Host Rock Properties (representing shale)		
Density[6]	2600	$kg\ m^{-3}$
Specific heat capacity[5]	960	$J\ kg^{-1}\ K^{-1}$
Thermal conductivity[5]	2.55	$W\ m^{-1}\ K^{-1}$
Porosity[6]	Ref fig	Ref fig
Permeability	Ref fig	Ref fig
Initial TOC[4]	0.05	1
Initial bound water content[2]	0.048	1
Tensile strength[8]	3	MPa
Enthalpy of mineral dehydration[1,2]	2800	$kJ\ kg(H_2O)^{-1}$
Enthalpy of organic cracking[1,2]	375	$kJ\ kg(TOC)^{-1}$
Brittle-ductile-transition[2]	500-750	°C

Sources:
[1]Aarnes et al. (2010), [2] Galerne and Hasenclever (2019), [3] Stern et al. (1975) ,[4] Spacapan et al. (2018), [5]Angenheister et al. (1982), [6] Rabbel (2017), [7] Spacapan et al. (2020), [8] Schön (2015)

3.4 Numerical Simulation: results

3.4.1 Impermeable sill: Flow around sill tip and methane plume

We first present and compare the results of the reference simulations of a 50 m thick, impermeable sill emplaced at 3 km depth in either a low-permeability (Figure 6) or high permeability (Figure 7) host rock. Figure 6 and 7 display the evolution of temperature, vitrinite reflectance (Ro) as proxy for thermal maturity (first row of images), pore fluid pressure (second row), permeability and transiently opened fracture porosity to highlight regions of active hydrofracturing (third row) and the methane fraction of the fluid (fourth row) in the model at 1, 60 and 1000 years after the sill is emplaced. Additionally, flow vectors colored by fluid velocity in the pore space are shown. We highly recommend to also view the movies supplied in the additional materials of this paper to get a better sense of the process dynamics in space and time.

One year after emplacement (left column in Figure 6 and 7), the sill is still over 1000°C hot and only the host rock within <10 m distance to the sill has been heated to temperatures of >350°C. Within the thin thermal aureole, thermal maturity increases strongly, methane is generated by thermal cracking and mineral dehydration takes place. Thermal expansion of the heated fluid, mineral dehydration and methane generation close to the sill lead to strongly elevated pore fluid pressures, which propagate away from the sill (Figure 6d and 7d). In both low- and high-permeability scenarios we observe similar peak pore pressures of around 80 – 85 MPa at the sill contact during the first weeks after the sill emplacement. However, in the high-permeability case (Figure 7d), the pressure front moves faster because of efficient fluid flow even far away from the sill. In contrast, the pressure front moves much slower in the low-permeability case (Figure 6d), where fast fluid flow is restricted to the region of active hydrofracturing (Figure 6g vs. 7g). Flow direction and therefore methane transport is sill-parallel towards the tips in the highly permeable contact aureole and radially outwards outside of the aureole (Figure 6d,j and 7d,j).

After 60 years of sill cooling (central column in Figure 6 and 7), the high-temperature aureole (>350°C) has expanded to ca. 25 m around the sill (Figure 6b and 7b), thermal maturity has reached Ro values above 2, which indicates the gas window or overmaturity. At this stage, pore pressure and permeability distribution in the two reference cases differ markedly. In the low-permeability host, fluid overpressure is still sufficiently high to cause hydrofracturing in a several 100 m wide halo around the sill, where permeability is elevated by 1-2 orders of magnitude with respect to background values (Figure 6e, h). Note that hydrofracturing is vanishing close to the sill where hydrofractures are closing again as pore pressure slowly reduces. The high-permeability host allows for a more efficient dissipation of fluid overpressures so that no more hydrofracturing occurs ca. 10 years after the sill emplacement. After 60 years, the remaining fluid overpressure around the sill is only a few MPa above hydrostatic (Figure 7e, h). Both models also develop porosity and permeability increase due to clay mineral dehydration, but this is limited to 50 m distance from the sill contact. In both models, the highest temperature in the inner aureole (ca. 10 m from contact) is reached ca. 10 years after the sill emplacement (around 670 ºC at the sill contact), while the outer aureole (up to ca. 50 m to contact) reaches its peak temperatures (300-400°C, depending on distance to sill) after around 60 years. The combined action of thermal contraction of the cooling fluid after reaching the peak-temperature and additional closure of hydrofractures (i.e., pore-space reduction) in the low-permeability host cause an inversion of the flow direction. After 60 years, fluids carrying high methane concentrations migrate towards the sill within a ~100 m thick region above and below the sill (Figure 6e,k, Figure 7e,k and supplementary movies). Despite the differences in permeability structure and pressure regimes, flow patterns of both reference simulations are relatively similar. The contact-parallel flow in the high permeability host is stronger, and these higher flow velocities lead to a more pronounced plume of rising methane on top of the sill near its tip (Figure 7k). Both cases also show a sizable methane accumulation remaining below the sill.

The right column in Figure 6 and 7 represents the end of the simulation after ca. 1000 years. The temperatures throughout the model are still elevated with respect to the initial geotherm but are now below 200°C everywhere. Fluid pressure in the low-permeability case is still up to 20 MPa above hydrostatic but has dropped below the failure criterion and hydrofracturing has stopped (Figure 6f,i). In the high-permeability host, pore pressure is reduced to values of <1 MPa above hydrostatic (Figure 7f). The dehydration-related permeability increase has not expanded significantly in either model. In the low-permeability scenario, some of the methane rises to 250 m above the sill, but the highest concentrations (almost pure methane, i.e., mass fraction close to 1) occur within 50–100 m to the sill contact (Figure 6l). In contrast, the model with a high-permeability host shows the formation of a localized secondary plume of very high methane concentrations (essentially pure methane) rising above the sill (Figure 7l), and the initial methane plume has reached ca. 400 m above the sill. The aureole below the sill has also accumulated high methane concentration in the fluids with up >70% methane fraction within 30 m of the sill. These methane-rich fluids remain trapped below the impermeable sill.

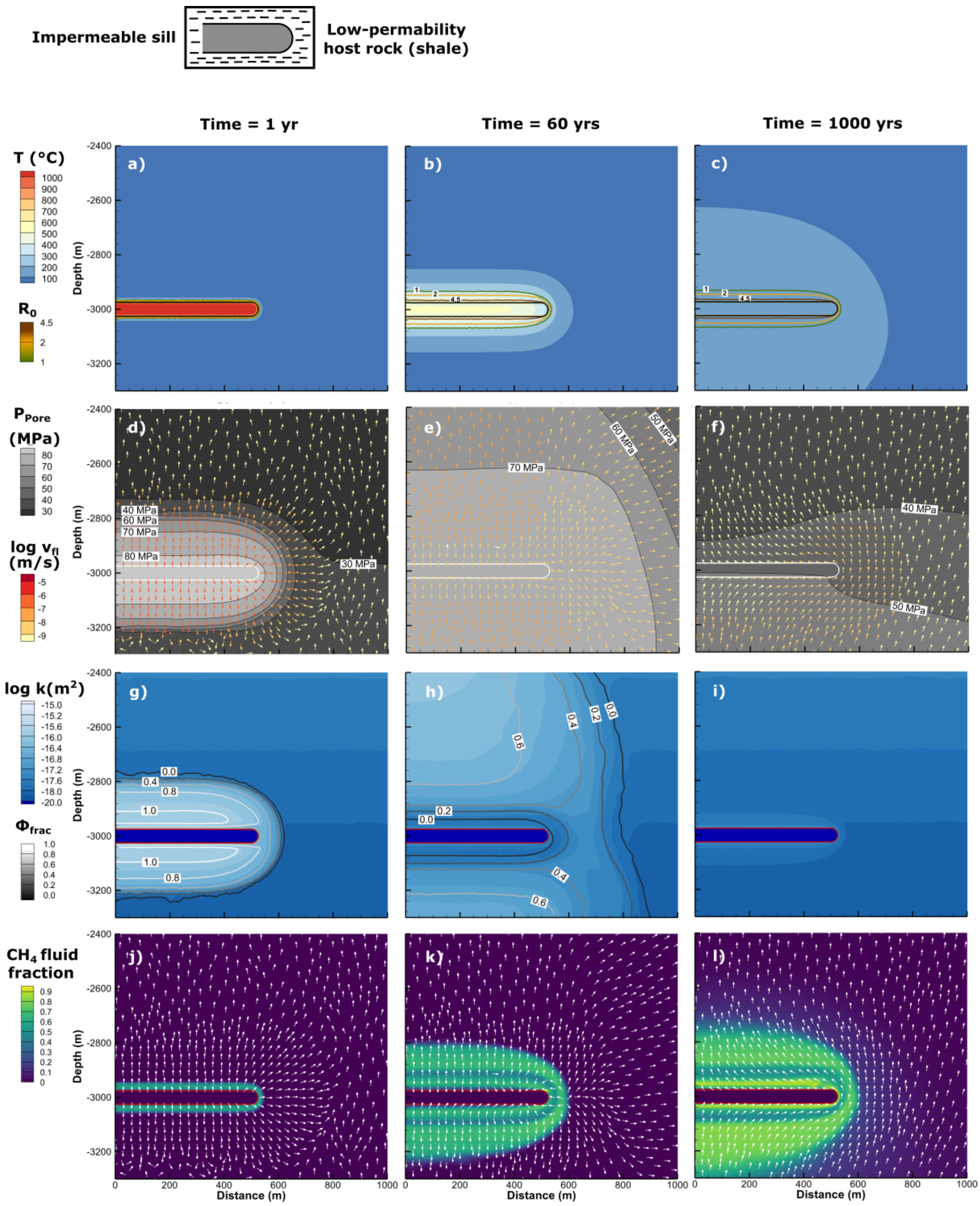

Figure 6. Reference simulation results for an impermeable sill of 50 m thickness at 3 km depth in the low-permeability host case. The columns correspond to 1, 60 and 1000 years of simulated time after emplacement, respectively. The rows represent four parameters characterizing thermal state, contact metamorphism and hydrothermal transport of methane: (a-c) Temperature, thermal maturity as vitrinite reflectance R_0 contours, (d-f) pore fluid pressure with flow vectors coloured by pore velocities, (g-i) permeability with fracture porosity contours, (j-l) methane fraction in fluid.

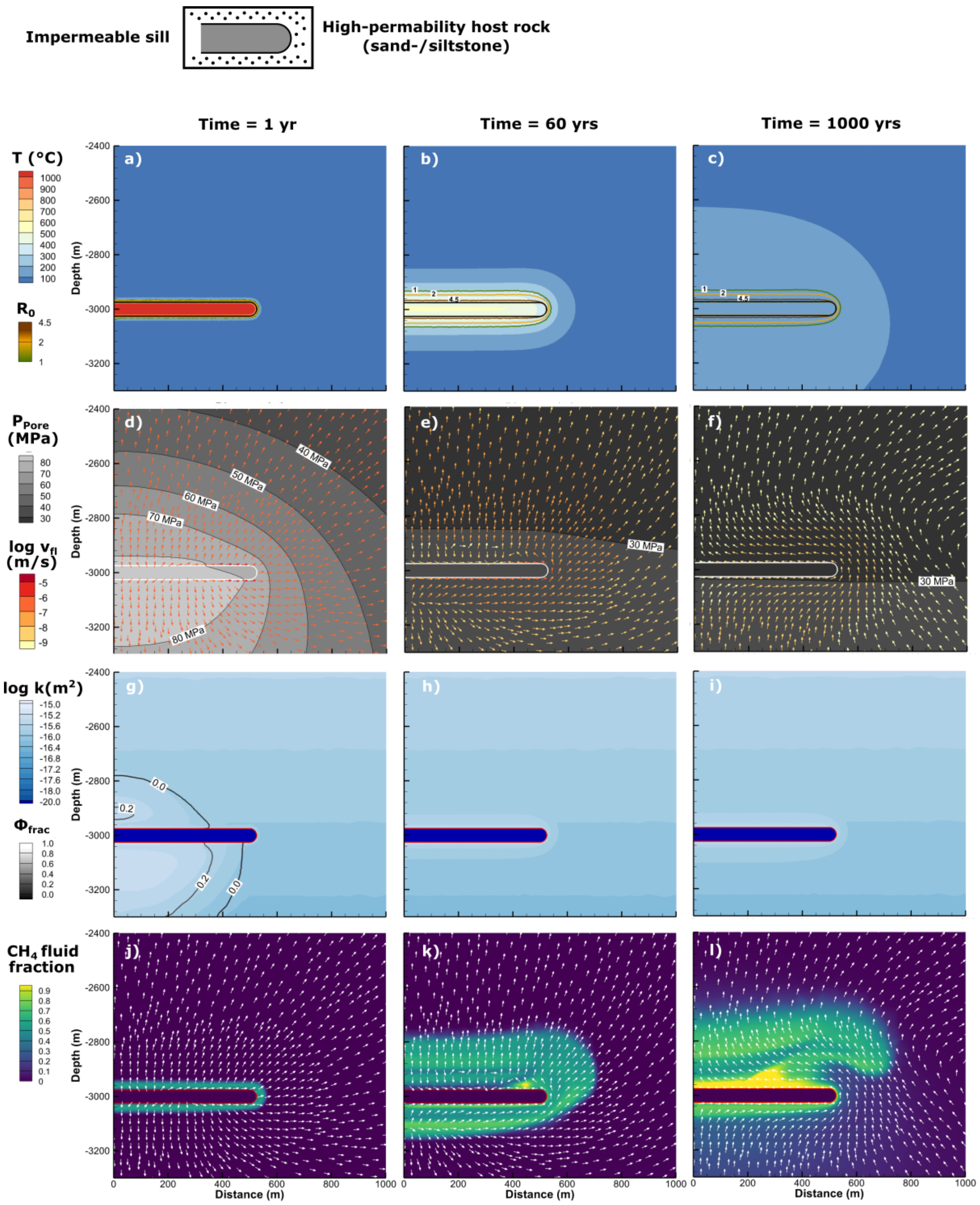

Figure 7. Reference simulation results for an impermeable sill of 50 m thickness at 3 km depth in the high-permeability host case. The columns correspond to 1, 60 and 1000 years of simulated time after emplacement, respectively. The rows represent four parameters characterizing thermal state, contact metamorphism and hydrothermal transport of methane: (a-c) Temperature, thermal maturity as vitrinite reflectance R_0 contours, (d-f) pore fluid pressure with flow vectors coloured by pore velocities, (g-i) permeability with fracture porosity contours, (j-l) methane fraction in fluid.

3.4.2 Permeable sill: Opened upward flow path and flow reversal

The introduction of cooling-related permeability generation in the sill profoundly changes the development of hydrothermal flow and methane transport patterns for both host rock types. We show identical parameters and time steps as for the reference simulations for low- and high-permeability host in Figure 8 and 9, respectively. To describe the details of the evolving flow patterns and hydrocarbon transport in the first 60 years, we add close-up figures for both cases displaying fluid pressure with flow vectors and permeability plots with (transient) fracture porosity (Figure 10). Finally, we quantify the total generated methane mass, the methane mass exposed to temperatures >400°C (graphitization conditions), the accumulation of methane in the permeable and porous sill, and the average sill temperature over time (Figure 11). Again, it is instructive to also view the supplementary movies for the respective simulations.

One year after emplacement, initial cooling of the sill leads to a progressing porosity/permeability front where the temperatures approach the solidus defined as 900°C (Figure 8 and 9, left column). At this stage, which continues until the sill becomes fully permeable, the simulations closely resemble the reference runs (see also supplementary animations of the simulations). Temperatures in the sediments are elevated only close to the intrusion, where the sediments almost instantly produce gas or become thermally overmature, i.e., vitrinite reflectance is larger than 1.5 (Figure 8a, 9a). Again, pore pressures are strongly elevated, and porosity and permeability in the sediments increase due to hydrofracturing around the sill (Figure 8d, g and 9d, g). Although large-scale methane distribution appears nearly identical to the reference scenarios, the detailed view shows that the onset of porosity and permeability generation in the sill's outermost regions allows flow within the sill (Figure 10, first and second column). Nevertheless, most fluid flow and methane transport is directed away from the sill contact with some sideways flow towards the sill tip along the bottom contact.

The entire sill has become fully porous and permeable after about 12 years (just after Figure 10, second column). While the same processes as described for the reference cases take place here as well (vanishing hydrofracturing, cooling of the contact aureole, fluid contraction and beginning inversion of the flow field towards the sill), the opening of the sill leads to stronger and more focused flow towards it. The flow direction below the sill changes from downward or contact-parallel to near-vertical upwards (Figure 8e, Figure 9e), "flushing" high methane concentrations directly into the sill (Figure 8k, 9k, 10c, i). However, at this point there are differences between the simulations considering a low- vs. high-permeability host rock.

In the low permeability case, a convection cell evolves within the sill, whose permeability is 2 – 3 orders of magnitude higher than that of the surrounding shale (Figure 10c). Methane transport into the sill is further enhanced by the much slower overpressure dissipation through this host rock and the fading hydrofracturing. After 60 years, hydrofracturing and the associated fracture porosity are progressively reduced and eventually stopped near the sill (Figure 8h, 10f), where fluid pressures have dropped below the failure criterium. The pressure drop is primarily caused by thermal contraction of the cooling fluids in the aureole and within the cooling sill. While the front of fading hydrofracturing and associated fracture porosity propagates away from the sill, methane-rich fluid is "squeezed" out of the host rock (Figure 8l, 10c, f) and contributes to a sustained flow and methane transport towards the sill. In this way, the sill is charged with up to 11,000 tons of methane (7.5% of total generated methane) within the first 100 years (Figure 11a). Methane mass in the cooling sill rises to ca. 16,000 tons (8.8% of total) after 250 years.

In the high permeability host rock, the porosity and permeability structure are much simpler, because hydrofracturing is absent due to generally lower fluid pressure (Figure 9e). The permeable sill and its dehydrated aureole, with slightly higher permeability than the background (Figure 9h, k, 10l), now represent an upward pathway and storage layer for methane-rich fluids. In addition to upward flow from below the sill, the flow directions at the intrusion tip also change and a circular flow pattern develops centered around a vortex located at the top of the intrusion tip (Figure 9e, 10i). This vortex initiates a sideward and downward directed flow that transports some of the methane from above and next to the sill tip back towards and into the sill tip (Figure 9k). During this phase of “methane flushing”, more methane enters the sill from below and through the tip than is lost through the top contact, and thus methane stored in the intrusion rises to 10,000 tons (6.3% of total) until ca. 90 years of simulation time (Figure 11b).

Interestingly, in both cases the average temperature in the sill during this stage of “flushing” is still between 400-800 °C (Figure 11). Thus, up to 7.5% of the overall generated methane that reaches the sill and the innermost 10 – 20 m of the aureole in the first ca. 100 years is exposed to these temperatures.

In the following phase until the end of both simulations, the sill and sediments cool down to below 200°C, thermal maturity increases only marginally, and fluid pressures dissipate to a level below the hydrofracturing point (right columns in Figures 8 and 9). In the simulation comprising a low-permeability host rock, highest methane concentrations accumulate within the sill or within 50 m of the upper contact (Figure 8l). In the high-permeability case, the release of methane previously trapped under the sill creates a slowly rising band of very high methane concentrations above the sill (Figure 9l). Flow velocities have further reduced by another 2 orders of magnitude, indicating that hydrothermal flow is stalling. In the last few hundred years of each simulation, the methane amount in the sill reduces to about 10,000 tons (5.5% of total) and 4000 tons (2.5% of total), respectively (Figure 11).

In summary, we identify three hydrothermal flow phases in the case of a sill with porosity and permeability evolution due to cooling joint formation. These include
(i) fluid flow and methane transport away from the sill and contact-parallel as long as the sill core is impermeable,
(ii) partial backflow and “methane-flushing” into, or through the sill once it is completely fractured; in low-permeability environments, this phase is accompanied by the closure of hydrofractures around the sill, thereby “squeezing out" methane-rich fluids that enter the sill
(iii) stabilization of hydrocarbon in and around the sill during fading hydrothermal circulation.

Despite the differences in the physical behavior between low- and high-permeability host rocks in phase (ii), i.e. fracture-facilitated fluid flow vs. matrix flow, substantial amounts of methane-rich fluids from below enter the porous and permeable sill shortly after its solidification at 900 °C. Compared to the simulations with impermeable sills, fluid overpressures dissipate slightly faster in the same host rock type, because the opening of pore space in the sill compensates for a small fraction of the overpressure.

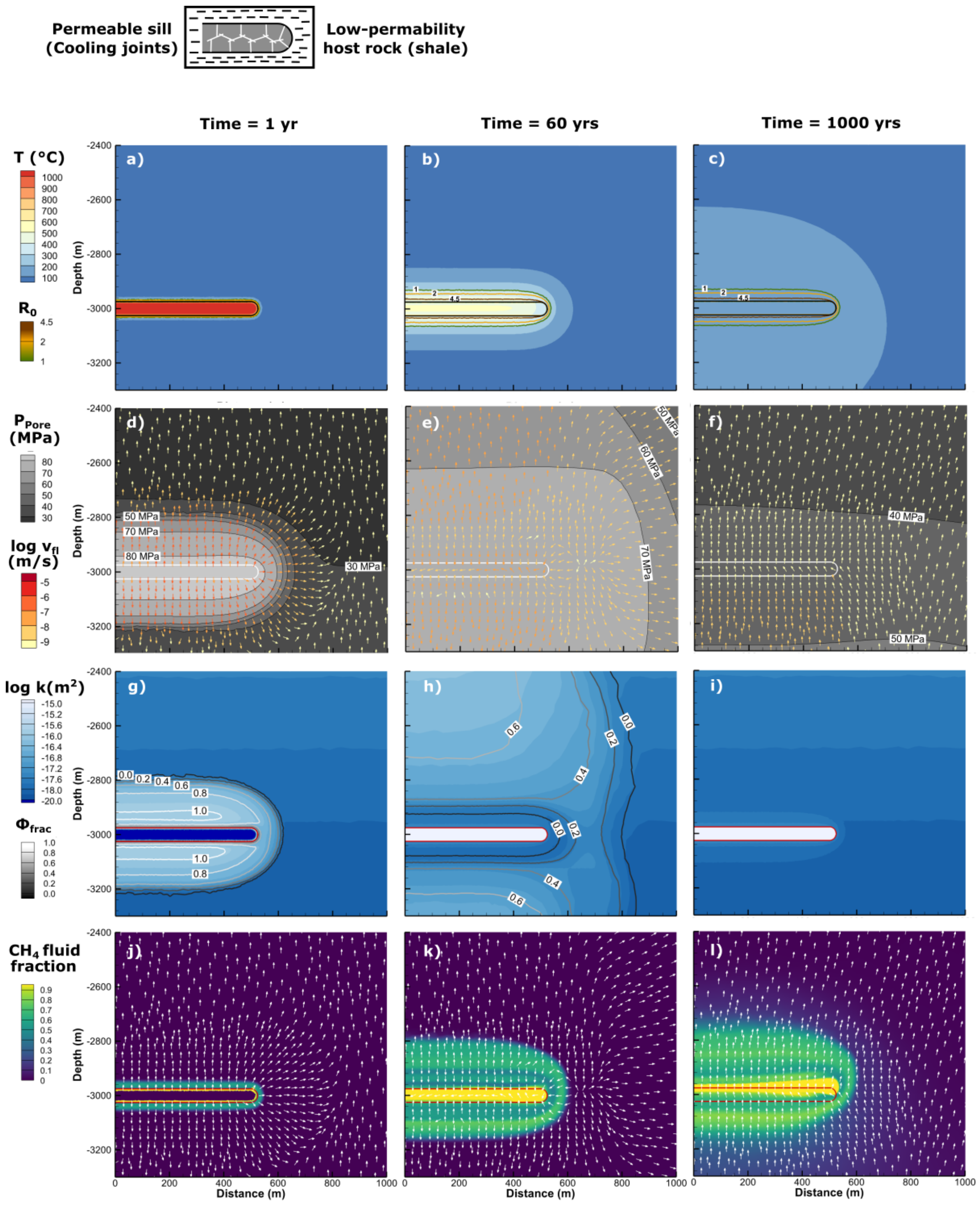

Figure 8. Simulation results for identical conditions as the reference case in Figure 6 (50 m thick, 3 km depth, low-permeability host), but the sill develops porosity and permeability with cooling. The rows represent four parameters characterizing thermal state, contact metamorphism and hydrothermal transport of methane: (a-c) Temperature, thermal maturity as vitrinite reflectance R_0 contours, (d-f) pore fluid pressure with flow vectors coloured by pore velocities, (g-i) permeability with fracture porosity contours, (j-l) methane fraction in fluid.

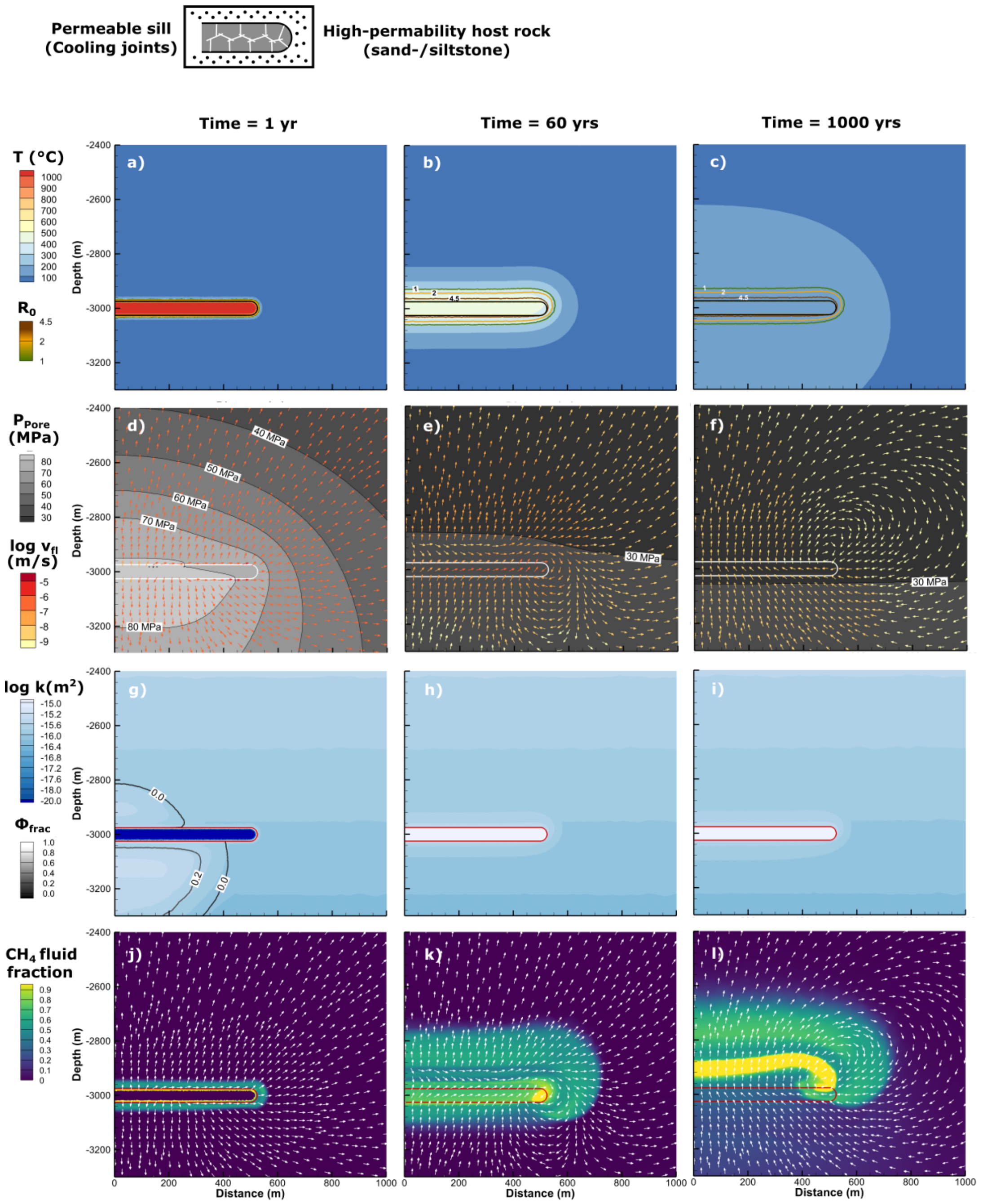

Figure 9. Simulation results for identical conditions as the reference case in Figure 7 (50 m thick, 3 km depth, high-permeability host), but the sill develops porosity and permeability with cooling. The columns correspond to 1, 60 and 1000 years of simulated time after emplacement, respectively. The rows represent four parameters characterizing thermal state, contact metamorphism and hydrothermal transport of methane: (a-c) Temperature, thermal maturity as vitrinite reflectance R_0 contours, (d-f) pore fluid pressure with flow vectors coloured by pore velocities, (g-i) permeability with fracture porosity contours, (j-l) methane fraction in fluid.

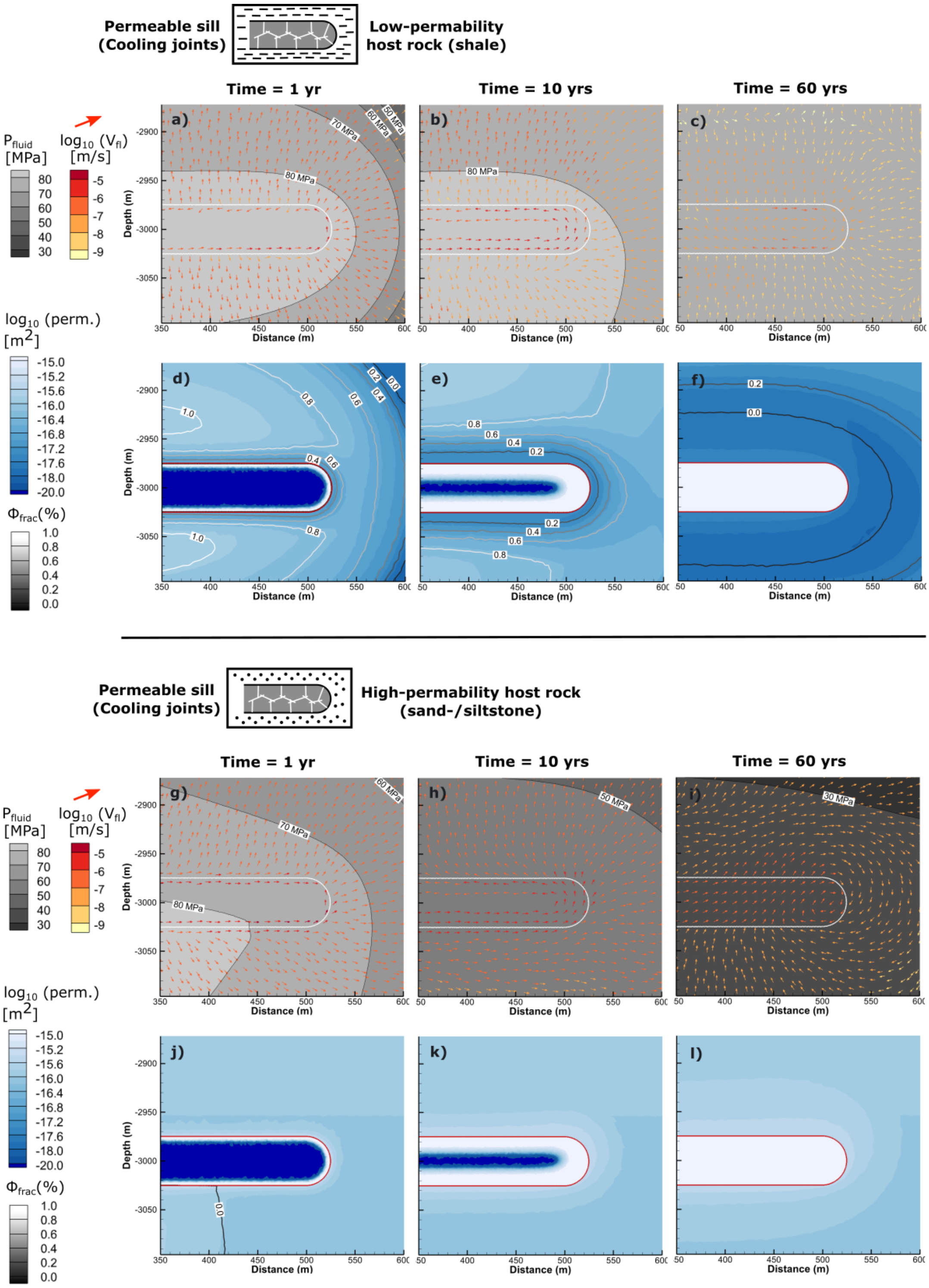

Figure 10. Close-up view of fluid pressure with flow vectors and permeability with fracture porosity contours at 1, 10 and 60 years of the permeable sill simulations in low-permeability (a-f) and high-permeability (g-l) host rocks.

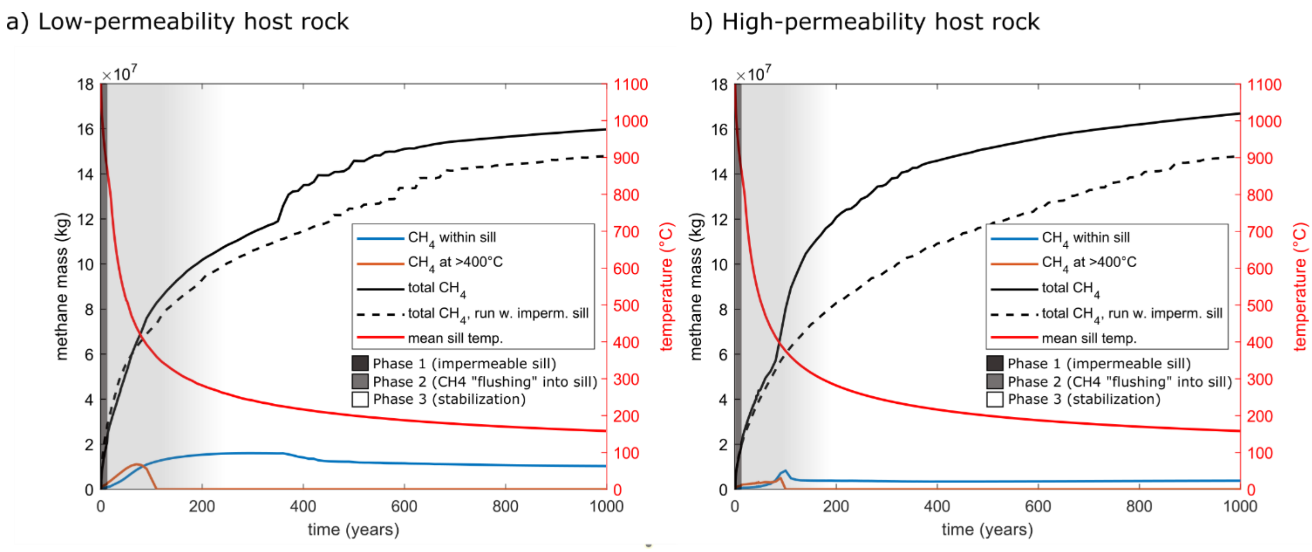

Figure 11. Cumulative methane mass for the simulations with permeable sills in low-permeability host (a) and high-permeability host (b) grouped by different criteria: within rock at >400 °C, i.e., sufficient for graphitization (orange line), within sill (blue line), total mass generated in the model (black line). Dotted black line gives the total generated methane mass for the respective reference simulation with an impermeable sill. Red line represents average sill temperature.

4 Interpretation and discussion

4.1 Hydrocarbon transport through hot sills

Outcrop data strongly suggests that transport of hydrocarbons generated around the sills in the northern Neuquén Basin occurs both vertically through the igneous intrusions as well as around their tip. Importantly, geochemical data from the study area suggests that the sills are responsible for most, if not all, organic matter transformation in the host rock, because background maturity between the sills is essentially zero (Spacapan et al., 2018; Rabbel et al., 2021). We thus interpret the observed hydrocarbons in the field to result from magmatic heating and hydrothermal activity rather than burial-related maturation.

Cooling joints and veins or dykes filled with black shale and bitumen are pervasive throughout the fracture networks of sills in our study area (Figure 2 and 3). The example shown in Figure 2 is particularly clear in showing the relationship between upwelling fluidized structures and the fill of the cooling joints. Note that similar observations have been documented in other outcrops at larger scales (Rabbel et al., 2021). We therefore propose that the flow of hot fluids and fluidized sediments through sills is a common occurrence in the northern Neuquén Basin. We thus provide solid outcrop evidence that sills can become preferred hydrocarbon transport pathways upon cooling. In contrast, this finding contradicts the widespread assumption of impermeable intrusions in modeling studies of hydrothermal fluid flow in volcanic basins (e.g., Iyer et al., 2013; Iyer et al., 2017; Galerne and Hasenclever, 2019).

Our observations complement numerous growing evidence that (carbon-rich) fluids or fluidized sediments entered sills of widely different sizes during their cooling stage, for instance in the Faroe-Shetland Basin (Rateau et al., 2013; Schofield et al., 2020), Karoo Basin (Svensen et al., 2010; Lenhard et al., 2023) and Guyamas Basin (Teske et al., 2021). Lenhard et al. (2023) concluded that carbon-rich fluids must have entered the sill during magma solidification, and Svensen et al. (2010) found metamorphosed sandstone dykes within dolerite sills in the Karoo Basin with mineral assemblage indicative of temperatures >300°C. They proposed that strong pressure gradients between the overpressured host rocks and the solidifying and contracting sill intrusions are likely responsible for liquefied sediments entering the intrusions shortly after cooling. Similar to this study, Svensen et al. (2010) based this interpretation on coupled thermo-hydraulic models, but explicitly considered thermal contraction of the magma. Although our approach of adding porosity to the sill is a simplification of this process, the general mechanism of hydrocarbon-rich fluids and sediments entering the cooling joint network in the intrusions in the Neuquén Basin is similar. We thus infer that our observations of hydrocarbon flow through hot sills in the Neuquén Basin are widespread in volcanic basins worldwide.

4.2 Impact of permeable sills on hydrothermal flow

Our numerical simulations allow us to assess the effects of porosity and permeability increase due to cooling joint formation when the sill has reached the solidus temperature. In simulations with an impermeable (i.e., unfractured) sill, the intrusion acts as a constant barrier for the hydrothermal flow and methane transport, while the aureole shows porosity and permeability evolution due to hydrofracturing and dehydration (Figure 6 and 7). In this configuration, an upward-rising methane plume initiates from the top contact of the sill. This plume is much more pronounced and methane is transported further upwards if the host rock is relatively permeable, such as silt- or sandstone (Figure 7). In addition, large amounts of methane are trapped below the sill, since no vertical pathways are available through the sill (Figure 6l and Figure 7l).

In contrast, a sill becoming permeable during cooling introduces drastic changes in the flow and methane transport patterns, and results in three phases with very different characteristics. The details of these phases differ depending on the type of host rock (low- vs. high-permeability), but share many similarities as described below.

Phase 1: Diverging and contact-parallel flow around the impermeable sill. Prior to complete solidification, the sill acts as a flow boundary and the flow patterns are essentially the same as for impermeable sills. Hydraulic fractures in the aureole and around the sill edge initiate in this early phase (Figure 10d, j), which may lead to the formation of the large bitumen dykes and calcite veins observed in the field (Figure 3). In addition, porosity generation inside the sill creates a suction effect that drives fluids into the intrusion (cf. Svensen et al., 2010).

Phase 2: Reversed flow and hydrothermal "flushing" of the solidified, permeable sill. The generation of cooling-related porosity and permeability inside the sill creates a hydraulic connection between the lower and upper aureole and initiates the abrupt change to vertical upflow into and through the sill (central column of Figure 8 and 9, Figure 10c, i). This rush of hydrocarbons (here: methane-rich fluids) into and through the sill occurs at average sill temperatures of 400–800 °C (Figure 11). Given the flow velocities and the timespan of methane accumulation (Figure 8k, Figure 9k, Figure 11), the model shows that fluids flowing through a 50 m thick sill are exposed to this high-temperature environment for tens of years, which could be sufficient for graphite generation and therefore seems to fit well with outcrop data and models for hydrothermal graphite generation (Figure 4; Rumble, 2014). We stress that this is also valid for low-permeability host rocks such as shale, because sustained hydrofracturing around the sill facilitates fluid flow by temporarily increasing porosity and permeability in the host rock (Figure 8, 10d, e). "Squeezing" of hydrocarbons towards the porous/permeable sill as the transiently opened fractures close corresponds well with the observation of multi-generation bitumen dykes/dyke arrays in the study area (e.g., Figure 3a, see also Rabbel et al. (2021)).

Phase 3: Stabilization of hydrocarbon and fading hydrothermal flow. In low-permeability host rocks, reversed flow towards the sill continues for a few hundred years and seems to be driven by closing of hydrofractures and thermal contraction of fluids within the still cooling sill (Figure 8l, 10c, supplementary movies). In high-permeability rocks, however, the sudden change in the pore pressure distribution due to porosity and permeability creation within the sill also initiates a vortex at the sill tip. This leads to transport of methane-rich fluids towards the sill tip from the surrounding host rock (Figure 9l). Eventually the amount of methane stabilizes within the sill (Figure 11). Hydrocarbons entering the sill in this last phase do not experience the extreme temperatures and are unlikely to experience graphitization.

4.3 Implications for flow and methane transport in volcanic basins

Our results have two main implications for fluid flow and methane transport in volcanic basins. First, they demonstrate that part of the generated methane may transform to graphite and thus be permanently stored in fractured sills. Second, the opening of vertical flow paths through fractured sills changes hydrocarbon migration routes compared to impermeable sills, and may thereby affect atmospheric degassing.

Despite observable differences in the physical processes at work during sill emplacement in low- vs. high-permeability host rocks, both environments allow for a signification amount of hydrocarbon flushing into a fractured sill at temperatures that are sufficient for graphitization. The occurrence of graphitic bitumen in dykes and as filling of cooling joints indicates that part of the carbon gases rising through permeable sills could be reduced to graphite and be stored as solids (Figure 2, 3, 11). Our results show a plausible mechanism for the creation of these features, as they demonstrate that methane-rich fluids can exploit hydrofractures to flow into the porous and permeable while temperatures in the sill are >400°C, i.e., high enough for graphite precipitation (Buseck and Beyssac, 2014). This fraction of the mobilized carbon is trapped permanently underground and is not available for degassing into the atmosphere. The widespread observations of graphite in the field suggests that a significant fraction of hydrocarbons maturated in the metamorphic aureoles of sills may not be transported away from the sill. Currently, the fraction of methane transformed to immobile graphite is not known. Our simulations with permeable sills provide a first estimate, showing that up to 10-11,000 tons (6.3-7.5%) of the generated methane experiences temperature >400°C (Figure 11a).

Sequestration of significant amounts of generated thermogenic carbon into cooling sills by secondary mineral formation is suggested by borehole data in the Karoo Basin, South Africa (Lenhardt et al., 2023). Despite this carbon mass not being available for degassing, a recent investigation on the Karoo Large Igneous Province and the related Toarcian crisis (ca 183 Ma) indicates that a total of ca. 20,500 Gt C is needed to replicate the Toarcian pCO2 and $\delta^{13}C$ proxy data (Heimdal et al., 2021). Based on existing quantitative model outcomes on the Karoo LIP (Galerne and Hasenclever, 2019), Lenhardt et al., (2023) pointed out that sequestration and degassing are not contradictory but rather point at synchronous processes during sill emplacement and cooling.

Additionally, permeable sills favor upward vertical flow and can thus contribute to fluid pressure release below the sill both in low-permeability and high-permeability host rocks. Conversely, impermeable sills favor sustained fluid pressure build-up below the sill and force contact-parallel fluid flow and methane transport towards sill tips (Iyer et al., 2017). These latter mechanisms, combined with a saucer-shaped sill geometry, are the main responsible for the formation of hydrothermal vent complexes at sill tips (Iyer et al., 2017; Galerne and Hasenclever, 2019). In line with field observations in the Neuquén Basin, the simulations considered here use relatively small, flat sills and therefore do not develop sufficient overpressure for hydrothermal vent formation (Galerne and Hasenclever, 2019; Spacapan et al., 2019). They are therefore not suited to quantify the effect of permeable and porous sills on venting. Nevertheless, the results allow us to speculate that for settings in which venting is generally more likely, permeable sills could reduce vent formation potential, or at least reduce atmospheric degassing. This is because the opening of vertical pathways through the sills offers a more direct fluid escape route and helps to dissipate overpressure below the sill.

4.4 Implications for igneous petroleum systems in the Río Grande Valley

Our study also provides further insight into the evolution of the igneous petroleum systems in the Río Grande Valley with respect to the timing of the charging of the igneous hydrocarbon reservoirs. The current conceptual models for these petroleum systems state that a first migration pulse of hydrocarbons into the reservoirs happens when cooling joints open (Witte et al., 2012; Spacapan et al., 2018; Spacapan et al., 2020). Our study demonstrates that hydrocarbons indeed migrate into the intrusions when the cooling joint network forms, but likely experience far too high temperatures (at least 400°C) for them to survive as producible liquids or gases (Figure 8, Figure 11a). Therefore, a survival of hydrocarbons entering the cooling joint network shortly after its creation seems highly unlikely. This result suggests that the igneous reservoirs are charged during the late-stage cooling of the sills, and after significant amounts of the hydrocarbons have flowed through the sills at high temperature. The migration model proposed earlier thus needs to be revised and split into two sub-stages: (1) a first influx of hydrocarbons through still hot sills, with no or very limited survival of hydrocarbons, and (2) a later migration of hydrocarbons within the cooled sill, where the hydrocarbons can survive and be trapped to form producible reservoirs.

4.5 Study limitations and future recommendations

Finally, we present selected recommendations for future work arising from the limitations of our study. Despite the complexity of the current numerical model, some known processes in the host rock are not yet considered. First, mineral precipitation at high temperatures can occur at non-negligible rates and lead to fast porosity-decrease, causing pore pressure increase and possibly fracturing (Townsend, 2018). In addition, buoyancy effects of methane or even two-phase flow are not considered, which may be an important parameter especially for venting (Iyer et al., 2017). Finally, we believe that due to the strong impact on hydrothermal flow patterns, future hydrothermal modelling studies of intrusion in sedimentary basins should consider the possibility of early porosity-permeability generation within the sills, especially in light of growing evidence for gas sequestration in sills worldwide. One important point would be to better constrain the permeability of sill fracture networks. Optimally, we should seek to reach beyond ad-hoc models and develop a physical model that quantifies porosity-permeability evolution under given conditions, e.g., depth, thickness, cooling rate, composition of magmatic intrusions.

5 Conclusions

We integrate geological field data with numerical models to investigate hydrothermal transport of hydrocarbon-rich fluids around fractured igneous sills. We use outcrops of fractured sills emplaced in organic-rich shales in the northern Neuquén Basin to establish that sills can become permeable fluid pathways upon solidification while still hot, which affects the fate of locally generated hydrocarbons. The numerical modelling study allows us to understand in detail the hydrothermal flow patterns in response to porosity and permeability generation inside a sill intrusion. This provides new insights into hydrothermal flow in volcanic sedimentary basins, because previous studies commonly assume that sills represent prominently impermeable bodies. The main conclusions of this study are as follows:

1. Widespread occurrence of veins with solid, strongly graphitized bitumen as well as cooling joints filled with solid bitumen or organic-rich shales evidence transport of hydrocarbon-rich fluids and liquefied sediments into the sill in a high-temperature (probably >350°C), high-pressure environment. This happens within years to several decades after solidification of the sill.

2. Numerical modelling indicates three flow phases around sills that become porous and permeable upon solidification, which differ markedly from flow around impermeable sills:

    (1) Contact-parallel flow toward the tip prior to solidification, creating an early plume above the sill tip.

(2) Sudden change to vertical flow upon complete solidification. This leads to flow of hydrocarbons from the lower contact aureole upwards into and/or through the sill (”flushing”). This effect is present in both low- and high-permeability host rocks, because hydrofracturing around the sill increases permeability and thus facilitates flow. In addition, hydrocarbons stored in closing hydrofractures are expelled, which, directly around the sill, pushes hydrocarbon-rich fluid back towards the sill.

(3) Stabilization of the flow regime with slow rise of hydrocarbon-rich fluids above the sill center, and backward-downward flow towards the sill due to either closing of hydrofractures (low-permeability host) or a vortex driven by the permeable sill (high-permeability host).

3. Simulations indicate that flow of methane through the sill occurs at temperatures >400°C, which meets the conditions for hydrothermal graphitization. This may explain field observations of graphitic bitumen dykes and could lead to permanent storage of part of the mobilized carbon (estimated up to 7.5%).

4. Thus, in contrast to proposed conceptual models, flow of hydrocarbons into newly formed cooling joints is likely not a viable migration/charge mechanism for sill reservoirs in the northern Neuquén Basin, as the intrusions are too hot for survival of liquid hydrocarbons.

5. Permeability creation with the cooling sills does not significantly reduce pressure build-up below the sill, but creates efficient upward pathways for fluid and reduces focusing of flow around the sill tip. With growing evidence for permeable sills in volcanic basins globally, the permeability evolution of sills should be addressed in future modelling studies focused on sill-related venting.

Author contributions

O. Rabbel: study concept design, field work, evaluation of field data, preparation and evaluation of numerical simulations, manuscript preparation and revision

J. Hasenclever: development of numerical code, preparation and evaluation of numerical simulations, preparation and revision of model description and results in manuscript

C. Y. Galerne: study concept design, preparation and evaluation of numerical simulations, manuscript preparation and revision

O. Galland: study concept design, field work and evaluation of field data, manuscript preparation and revision

K. Mair: study concept design, field work and evaluation of field data, manuscript preparation and revision

O. Palma: field work, geochemical analysis, evaluation of field data, manuscript preparation and revision

Acknowledgements

Rabbel's position was funded by the Faculty of Mathematics and Natural Science of the University of Oslo, through the "Earth Flows" Strategic Initiative project. The DEEP Research School provided funding for fieldwork (249040/F60). We thank YTEC for providing Raman analyses of the graphitic bitumen.

Supplementary material

Additional figures and animations of all described simulation runs, plus some additional ones using a thinner sill, can be found in the following FAIR data repository: https://osf.io/28whp/?view_only=5ad1d2cc52844f1cb715516d076a5dd0

Competing interests

The authors declare that they have no conflict of interest.

References

Aarnes, I., Podladchikov, Y.Y., Svensen, H., 2012. Devolatilization-induced pressure build-up: Implications for reaction front movement and breccia pipe formation. Geofluids 12, 265-279, 10.1111/j.1468-8123.2012.00368.x.

Aarnes, I., Svensen, H., Connolly, J.A.D., Podladchikov, Y.Y., 2010. How contact metamorphism can trigger global climate changes: Modeling gas generation around igneous sills in sedimentary basins. Geochimica et Cosmochimica Acta 74, 7179-7195, http://dx.doi.org/10.1016/j.gca.2010.09.011.

Angenheister, G., Cermak, V., Huckenholz, H., Rybach, L., Schmid, R., Schopper, J., Schuch, M., Stoeffler, D., Wohlenberg, J., 1982. Physical properties of rocks. Subvol. a.

Beyssac, O., Goffé, B., Chopin, C., Rouzaud, J.N., 2002. Raman spectra of carbonaceous material in metasediments: a new geothermometer. Journal of Metamorphic Geology 20, 859-871, 10.1046/j.1525-1314.2002.00408.x.

Buseck, P.R., Beyssac, O., 2014. From organic matter to graphite: Graphitization. Elements 10, 421-426.

Chevallier, L., Gibson, L.A., HNhleko, L.O., Woodford, A.C., Nomquphu, W., Kippie, I., 2004. Hydrogeology of fractured-rock aquifers and related ecosystems within the Qoqodala dolerite ring and sill complex, Great Kei catchment, Eastern Cape, Water Res. Com., S. Afr., p. 127.

Cobbold, P.R., Diraison, M., Rossello, E.A., 1999. Bitumen veins and Eocene transpression, Neuquén basin, Argentina. Tectonophysics 314, 423-442.

Combina, A., Nullo, F., 2005. Tertiary volcanism and sedimentation in the southern Cordillera Principal, Mendoza, Argentina, Extended Abstracts, 6th International Symposium on Andean Geodynamics, pp. 174-177.

Connolly, J., 2009. The geodynamic equation of state: what and how. Geochemistry, Geophysics, Geosystems 10.

Delaney, P.T., 1982. Rapid intrusion of magma into wet rock: Groundwater flow due to pore pressure increases. Journal of Geophysical Research: Solid Earth 87, 7739-7756.

Einsele, G., Gieskes, J.M., Curray, J., Moore, D.M., Aguayo, E., Aubry, M.-P., Fornari, D., Guerrero, J., Kastner, M., Kelts, K., Lyle, M., Matoba, Y., Molina-Cruz, A., Niemitz, J., Rueda, J., Saunders, A., Schrader, H., Simoneit, B., Vacquier, V., 1980. Intrusion of basaltic sills into highly porous sediments, and resulting hydrothermal activity. Nature 283, 441-445, doi: 10.1038/283441a0.

Galerne, C.Y., Hasenclever, J., 2019. Distinct Degassing Pulses During Magma Invasion in the Stratified Karoo Basin—New Insights From Hydrothermal Fluid Flow Modeling. Geochemistry, Geophysics, Geosystems 20, 2955-2984, 10.1029/2018GC008120.

Hayba, D. O., and S. E. Ingebritsen, 1997. Multiphase groundwater flow near cooling plutons, J. Geophys. Res., 102, 12,235–12,252, doi:10.1029/97JB00552.

Hays, W.W., Nuttli, O.W., Scharon, L., 1967. Mapping gilsonite veins with the electrical resistivity method. Geophysics 32, 302-310.

Heimdal, T. H., Goddéris, Y., Jones, M. T., & Svensen, H. H., 2021. Assessing the importance of thermogenic degassing from the Karoo Large Igneous Province (LIP) in driving Toarcian carbon cycle perturbations. Nature Communications, 12(1), 6221.Hetényi, G., Taisne, B., Garel, F., Médard, É., Bosshard, S., Mattsson, H.B., 2012. Scales of columnar jointing in igneous rocks: field measurements and controlling factors. Bulletin of Volcanology 74, 457-482, 10.1007/s00445-011-0534-4.

Howell, J.A., Schwarz, E., Spalletti, L.A., Veiga, G.D., 2005. The Neuquén Basin: an overview, in: Veiga, G.D., Spalletti, L.A., Howell, J.A., Schwarz, E. (Eds.), Geological Society, London, Special Publications, 252, pp. 1-14.

Ingebritsen, S. E., Geiger, S., Hurwitz, S., & Driesner, T., 2010. Numerical simulation of magmatic hydrothermal systems. Reviews of Geophysics, 48(1).

Iyer, K., Rüpke, L., Galerne, C.Y., 2013. Modeling fluid flow in sedimentary basins with sill intrusions: Implications for hydrothermal venting and climate change. Geochemistry, Geophysics, Geosystems 14, 5244-5262, 10.1002/2013GC005012.

Iyer, K., Schmid, D.W., Planke, S., Millett, J., 2017. Modelling hydrothermal venting in volcanic sedimentary basins: Impact on hydrocarbon maturation and paleoclimate. Earth Planet. Sci. Lett. 467, 30-42

Jamtveit, B., Svensen, H., Podladchikov, Y.Y., Planke, S., 2004. Hydrothermal vent complexes associated with sill intrusions in sedimentary basins. Physical Geology of High-Level Magmatic Systems. Geological Society, London, Special Publications 234, 233-241.

Kay, S.M., Burns, W.M., Copeland, P., Mancilla, O., 2006. Upper Cretaceous to Holocene magmatism and evidence for transient Miocene shallowing of the Andean subduction zone under the northern Neuquén Basin. Geological Society of America Special Papers 407, 19-60.

Kietzmann, D.A., Palma, R.M., Riccardi, A.C., Martín-Chivelet, J., López-Gómez, J., 2014. Sedimentology and sequence stratigraphy of a Tithonian–Valanginian carbonate ramp (Vaca Muerta Formation): a misunderstood exceptional source rock in the Southern Mendoza area of the Neuquén Basin, Argentina. Sedimentary geology 302, 64-86.

Kobchenko, M., Hafver, A., Jettestuen, E., Renard, F., Galland, O., Jamtveit, B., Meakin, P., Dysthe, D. K., 2014. Evolution of a fracture network in an elastic medium with internal fluid generation and expulsion. Physical Review E, 90(5), 052801.

Kwiecinska, B., Suárez-Ruiz, I., Paluszkiewicz, C., Rodriques, S., 2010. Raman spectroscopy of selected carbonaceous samples. International Journal of Coal Geology 84, 206-212.

Lenhardt, N., Galerne, C., Le Roux, P., Götz, A. E., & Lötter, F. J., 2023. Geochemistry of dolerite intrusions of the southeastern Main Karoo Basin, South Africa: Magma evolution, evidence for thermogenic gas sequestration, and potential implications for the early Toarcian Oceanic Anoxic Event, Gondwana Research, 113, 144-162.

Manceda, R., Figueroa, D., 1995. Inversion of the Mesozoic Neuquén rift in the Malargüe fold and thrust belt, Mendoza, Argentina, in: Tankard, A.J., S., S., Welsink, H.J. (Eds.), Petroleum basins of South America: AAPG Memoir, 62, pp. 369–382.

Mark, N., Schofield, N., Pugliese, S., Watson, D., Holford, S., Muirhead, D., Brown, R., Healy, D., 2018. Igneous intrusions in the Faroe Shetland basin and their implications for hydrocarbon exploration; new insights from well and seismic data. Marine and Petroleum Geology 92, 733-753.

Marsh, B.D., 2002. On bimodal differentiation by solidification front instability in basaltic magmas, part 1: basic mechanics. Geochimica et Cosmochimica Acta 66, 2211-2229, https://doi.org/10.1016/S0016-7037(02)00905-5.
Nermoen, A., Galland, O., Jettestuen, E., Fristad, K., Podladchikov, Y.Y., Svensen, H., Malthe-Sørenssen, A., 2010. Experimental and analytic modeling of piercement structures. J. Geophys. Res. 115, B10202, 10.1029/2010jb007583.
Palma, J.O., Spacapan, J.B., Rabbel, O., Galland, O., Ruiz, R., Leanza, H.A., 2019. The atypical igneous Petroleum System of the Cara Cura range, southern Mendoza province, Argentina, in: The Physical Geology of Subvolcanic Systems: Laccoliths, Sills and Dykes (LASI6), Book The atypical igneous Petroleum System of the Cara Cura range, southern Mendoza province, Argentina, Edition ed.
Panahi, H., Kobchenko, M., Meakin, P., Dysthe, D.K., Renard, F., 2018. In-situ imaging of fracture development during maturation of an organic-rich shale: Effects of heating rate and confinement. Marine and Petroleum Geology 95, 314-327.
Parnell, J., & Carey, P. F., 1995. Emplacement of bitumen (asphaltite) veins in the Neuquén Basin, Argentina, AAPG bulletin, 79(12), 1798-1816.
Petford, N., 2003. Controls on primary porosity and permeability development in igneous rocks. Hydrocarbons in Crystalline Rocks 214, 93-107, Doi 10.1144/Gsl.Sp.2003.214.01.06.
Potgieter-Vermaak, S., Maledi, N., Wagner, N., Van Heerden, J., Van Grieken, R., Potgieter, J., 2011. Raman spectroscopy for the analysis of coal: a review. Journal of Raman Spectroscopy 42, 123-129.
Rabbel, O., 2017. Integrated Seismic and Rock Physics Modelling of Oil-Producing Volcanic Sills in the Neuquén Basin, Argentina, Department of Geosciences. University of Oslo, Oslo, p. 83.
Rabbel, O., Galland, O., Mair, K., Lecomte, I., Senger, K., Spacapan, J.B., Manceda, R., 2018. From field analogues to realistic seismic modelling: a case study of an oil-producing andesitic sill complex in the Neuquén Basin, Argentina. J. Geol. Soc., 10.1144/jgs2017-116.
Rabbel, O., Mair, K., Galland, O., Grühser, C., Meier, T., 2020. Numerical modeling of fracture network evolution in organic-rich shale with rapid internal fluid generation. Journal of Geophysical Research: Solid Earth 125, e2020JB019445.
Rabbel, O., Palma, J.O., Mair, K., Galland, O., Spacapan, J.B., Senger, K., 2021. Fracture networks in shale-hosted igneous intrusions: Processes, distribution and implications for igneous petroleum systems. J. Struct. Geol. 150, 104403
Rantitsch, G., Lämmerer, W., Fisslthaler, E., Mitsche, S., Kaltenböck, H., 2016. On the discrimination of semi-graphite and graphite by Raman spectroscopy. International Journal of Coal Geology 159, 48-56.
Rateau, R., Schofield, N., Smith, M., 2013. The potential role of igneous intrusions on hydrocarbon migration, West of Shetland. Petroleum Geoscience 19, 259-272, doi: 10.1144/petgeo2012-035.
Rodriguez Monreal, F., Villar, H.J., Baudino, R., Delpino, D., Zencich, S., 2009. Modeling an atypical petroleum system: A case study of hydrocarbon generation, migration and accumulation related to igneous intrusions in the Neuquen Basin, Argentina. Marine and Petroleum Geology 26, 590-605, doi: 10.1016/j.marpetgeo.2009.01.005.
Rumble, D., 2014. Hydrothermal graphitic carbon. Elements 10, 427-433.
Schiuma, M.F., 1994. Intrusivos del valle del Río Grande, provincia de Mendoza, su importancia como productores de hidrocarburos. Universidad Nacional de La Plata.
Schofield, N., Holford, S., Edwards, A., Mark, N., Pugliese, S., 2020. Overpressure transmission through interconnected igneous intrusions. AAPG Bulletin 104, 285-303.
Schön, J.H., 2015. Physical properties of rocks: Fundamentals and principles of petrophysics. Elsevier.
Senger, K., Millett, J., Planke, S., Ogata, K., Eide, C., Festøy, M., Galland, O., Jerram, D.A., 2017. Effects of igneous intrusions on the petroleum system: a review. First Break 35.6, 47-56, 10.3997/1365-2397.2017011.

Spacapan, J.B., D'Odorico, A., Palma, O., Galland, O., Rojas Vera, E., Ruiz, R., Leanza, H.A., Medialdea, A., Manceda, R., 2020. Igneous petroleum systems in the Malargüe fold and thrust belt, Río Grande Valley area, Neuquén Basin, Argentina. Marine and Petroleum Geology 111, 309-331, https://doi.org/10.1016/j.marpetgeo.2019.08.038.

Spacapan, J.B., D´Odorico, A., Palma, O., Galland, O., Senger, K., Ruiz, R., Manceda, R., Leanza, H.A., 2019. Low resistivity zones at contacts of igneous intrusions emplaced in organic-rich formations and their implications on fluid flow and petroleum systems: A case study in the northern Neuquén Basin, Argentina. Basin Research, 10.1111/bre.12363.

Spacapan, J.B., Galland, O., Leanza, H.A., Planke, S., 2017. Igneous sill and finger emplacement mechanism in shale-dominated formations: a field study at Cuesta del Chihuido, Neuquén Basin, Argentina. J. Geol. Soc. 174, 422-433, 10.1144/jgs2016-056.

Spacapan, J.B., Palma, O., Galland, O., Manceda, R., Rocha, E., D'Odorico, A., Leanza, H.A., 2018. Thermal impact of igneous sill complexes on organic-rich formations and the generation of a petroleum system: case study in the Neuquén Basin, Argentina. Mar. Pet. Geol. 91, 519-531, https://doi.org/10.1016/j.marpetgeo.2018.01.018.

Stern, C.R., Huang, W.-L., Wyllie, P.J., 1975. Basalt-andesite-rhyolite-H2O: Crystallization intervals with excess H2O and H2O-undersaturated liquidus surfaces to 35 kolbras, with implications for magma genesis. Earth and Planetary Science Letters 28, 189-196.

Svensen, H., Aarnes, I., Podladchikov, Y.Y., Jettestuen, E., Harstad, C.H., Planke, S., 2010. Sandstone dikes in dolerite sills: Evidence for high-pressure gradients and sediment mobilization during solidification of magmatic sheet intrusions in sedimentary basins. Geosphere 6, 211-224.

Svensen, H., Planke, S., Malthe-Sørenssen, A., Jamtveit, B., Myklebust, R., Rasmussen Eidem, T., Rey, S.S., 2004. Release of methane from a volcanic basin as a mechanism for initial Eocene global warming. Nature 429, 542-545, doi: 10.1038/nature02566.

Sweeney, J.J., Burnham, A.K., 1990. Evaluation of a simple model of vitrinite reflectance based on chemical kinetics. AAPG bulletin 74, 1559-1570.

Teske A, Lizarralde D, Höfig TW, and the Expedition 385 Scientists (2021): Expedition 385 Summary. Proceedings of the International Ocean Discovery Program 385.

doi: 10.14379/iodp.proc.385.101.2021Townsend, M.R., 2018. Modeling Thermal Pressurization Around Shallow Dikes Using Temperature-Dependent Hydraulic Properties: Implications for Deformation Around Intrusions. Journal of Geophysical Research: Solid Earth 123, 311-323.

Witte, J., Bonora, M., Carbone, C., Oncken, O., 2012. Fracture evolution in oil-producing sills of the Rio Grande Valley, northern Neuquen Basin, Argentina. AAPG Bulletin 96, 1253-1277, doi: 10.1306/10181110152.

Yagupsky, D.L., Cristallini, E.O., Fantín, J., Valcarce, G.Z., Bottesi, G., Varadé, R., 2008. Oblique half-graben inversion of the Mesozoic Neuquén Rift in the Malargüe Fold and Thrust Belt, Mendoza, Argentina: New insights from analogue models. Journal of Structural Geology 30, 839-853, https://doi.org/10.1016/j.jsg.2008.03.007.

Zanella, A., Cobbold, P.R., Ruffet, G., Leanza, H.A., 2015. Geological evidence for fluid overpressure, hydraulic fracturing and strong heating during maturation and migration of hydrocarbons in Mesozoic rocks of the northern Neuquén Basin, Mendoza Province, Argentina. J. S. Amer. Earth. Sci. 62, 229-242, http://dx.doi.org/10.1016/j.jsames.2015.06.006.